Czech Technical University in Prague
Faculty of Nuclear Sciences and Physical Engineering

Department of Physics
Study programme: Nuclear and Particle Physics

Impact of Propagation of Cosmic Rays on their Properties Measured at the Highest Energies

DIPLOMA THESIS

Author:	Bc. Robert Hrubý
Supervisor:	Ing. Jakub Vícha, Ph.D.
Consultant	Ing. Alena Bakalová
Academic year:	2023/2024

České vysoké učení technické v Praze
Fakulta jaderná a fyzikálně inženýrská

Katedra fyziky
Studijní program: Jaderná a částicová fyzika

Vliv šíření kosmického záření na jeho vlastnosti pozorované na nejvyšších energiích

DIPLOMOVÁ PRÁCE

Vypracoval:	Bc. Robert Hrubý
Vedoucí práce:	Ing. Jakub Vícha, Ph.D.
Konzultant:	Ing. Alena Bakalová
Rok:	2023/2024

ČVUT
ČESKÉ VYSOKÉ UČENÍ TECHNICKÉ V PRAZE

ZADÁNÍ DIPLOMOVÉ PRÁCE

I. OSOBNÍ A STUDIJNÍ ÚDAJE

Příjmení: **Hrubý** Jméno: **Robert** Osobní číslo: **503096**

Fakulta/ústav: **Fakulta jaderná a fyzikálně inženýrská**

Zadávající katedra/ústav: **Katedra fyziky**

Studijní program: **Jaderná a částicová fyzika**

II. ÚDAJE K DIPLOMOVÉ PRÁCI

Název diplomové práce:

Vliv šíření kosmického záření na jeho vlastnosti pozorované na nejvyšších energiích

Název diplomové práce anglicky:

Impact of Propagation of Cosmic Rays on their Properties Measured at the Highest Energies

Pokyny pro vypracování:

1) Simulace propagace kosmického záření pro různé částice a vlastnosti jejich zdrojů pomocí programu CRPropa 3.
2) Studium měřených vlastností kosmického záření ultra-vysokých energií.
3) Hledání vlastností zdrojů kosmického záření, které jsou v souladu s měřeními Observatoře Pierra Augera ohledně anizotropie, složení a energetického spektra.

Seznam doporučené literatury:

[1] A. Aab, et al.: Measurement of the cosmic ray energy spectrum above 2.5 x 10^18 eV using the Pierre Auger Observatory, Phys. Rev. D 102 (2020) 062005
[2] A. Aab, et al.: Indication of anisotropy in arrival directions of ultra-high-energy cosmic rays through comparison to the flux pattern of extragalactic gamma-ray sources, Astrophys. J. Lett. 853 (2018) L29
[3] A. Aab, et al.: Depths of maximum of air-shower profiles at the Pierre Auger Observatory: Composition implications, Phys. Rev. D 90 (2014) 122006
[4] Ch. Ding, et al.: The imprint of large scale structure on the ultra-high-energy cosmic ray sky, Astrophys. J. Lett. 913 (2021) L13
[5] R. A. Batista, et al., CRPropa 3 - a public astrophysical simulation framework for propagating extraterrestrial ultra-high energy particles, JCAP 05 (2016) 038.

Jméno a pracoviště vedoucí(ho) diplomové práce:

Ing. Jakub Vícha, Ph.D. Fyzikální ústav AV ČR, v.v.i.

Jméno a pracoviště druhé(ho) vedoucí(ho) nebo konzultanta(ky) diplomové práce:

Ing. Alena Bakalová katedra fyziky FJFI

Datum zadání diplomové práce: **31.10.2023** Termín odevzdání diplomové práce: **10.05.2024**

Platnost zadání diplomové práce: **31.10.2025**

Ing. Jakub Vícha, Ph.D.
podpis vedoucí(ho) práce

podpis vedoucí(ho) ústavu/katedry

doc. Ing. Václav Čuba, Ph.D.
podpis děkana(ky)

III. PŘEVZETÍ ZADÁNÍ

Diplomant bere na vědomí, že je povinen vypracovat diplomovou práci samostatně, bez cizí pomoci, s výjimkou poskytnutých konzultací.
Seznam použité literatury, jiných pramenů a jmen konzultantů je třeba uvést v diplomové práci.

10. 11. 2023
Datum převzetí zadání

Podpis studenta

ČESKÉ VYSOKÉ UČENÍ TECHNICKÉ V PRAZE
Fakulta jaderná a fyzikálně inženýrská

Břehová 7
115 19 Praha 1

P R O H L Á Š E N Í

Já, níže podepsaný

Jméno a příjmení studenta:	Robert Hrubý
Osobní číslo:	503096
Studijní program:	Jaderná a částicová fyzika
Studijní obor:	/
Specializace:	/

prohlašuji, že jsem diplomovou práci s názvem:

Vliv šíření kosmického záření na jeho vlastnosti pozorované na nejvyšších energiích

vypracoval samostatně a uvedl veškeré použité informační zdroje v souladu s Metodickým pokynem o dodržování etických principů při přípravě vysokoškolských závěrečných prací.

Rovněž souhlasím s porovnáním textu mé kvalifikační práce s databází kvalifikačních prací Theses.cz provozovanou Národním registrem vysokoškolských kvalifikačních prací a systémem na odhalování plagiátů.

V Praze dne 01/01/24 ....

podpis

Poděkování

Rád bych poděkoval Ing. Jakubu Víchovi, Ph.D., a Ing. Aleně Bakalové za jejich rady a obrovskou pomoc v průběhu celé práce.

Rád bych také poděkoval Ing. Markovi Birošovi za pomoc, diskuse a rady.

Dále bych chtěl poděkovat Honzovi Podiukovi za neustálou podporu a v neposlední řadě svým rodičům, bez kterých by nic z tohoto nebylo možné.

Bc. Robert Hrubý

Název práce:
Vliv šíření kosmického záření na jeho vlastnosti pozorované na nejvyšších energiích
Autor: Bc. Robert Hrubý

Studijní program: Jaderná a částicová fyzika
Druh práce: Diplomová práce

Vedoucí práce: Ing. Jakub Vícha, Ph.D.
Oddělení astročásticové fyziky, Fyzikální ústav Akademie věd České republiky, v. v. i.
Konzultant: Ing. Alena Bakalová
Oddělení astročásticové fyziky, Fyzikální ústav Akademie věd České republiky, v. v. i.

Abstrakt: Studie zkoumala chování extragalaktického kosmického záření v energiích nad 40 EeV pomocí simulací v programu CRPropa 3. Při analýze byly zkoumány dva různé případy umožňující nalézt anizotropní signál: výběr nad a pod galaktickou rovinou a výběr vzhledem k pozorovanému dipólu ve směrech příletů kosmického záření. V případě výběru nad a pod galaktickou rovinou nebyl pozorován žádný významný hmotnostní rozdíl. Při rozdělení podle pozorovaného dipólu se ukazuje vyšší citlivost v hmotnostním rozdílu, nicméně rozdíly nedosahují hodnot pozorovaných Observatoří Pierra Augera. Dále byl testován vliv změny pozice extragalaktického dipólu, kde se ukázalo, že má vliv na anizotropii v hmotnostním rozdílu.

Klíčová slova: Kosmické záření ultra-vysokých energií, šíření kosmického záření, hloubka maxima spršky, velkoškálová anizotropie, galaktické magnetické pole.

Title:
Impact of Propagation of Cosmic Rays on their Properties Measured at the Highest Energies
Author: Bc. Robert Hrubý

Abstract: The study investigated the behaviour of extragalactic cosmic rays at energies above 40 EeV using simulations in CRPropa 3. The analysis examined two different cases allowing to find an anisotropic signal: selection above and below the galactic plane and selection relative to the observed dipole in the directions of cosmic ray arrivals. In the case of selection above and below the galactic plane, no significant mass difference was observed. However, selection according to the dipole shows a higher sensitivity in the mass difference. However, the difference does not reach the values observed by the Pierre Auger Observatory. Furthermore, the effect of changing the extragalactic dipole position was investigated and found to have an effect on the anisotropy in the mass difference.

Key words: Ultra-high energy cosmic rays, cosmic ray propagation, shower maximum depth, large-scale anisotropy, galactic magnetic field.

Contents

Introduction

It has been a long time since the discovery of cosmic rays and even the recent ultra-high-energy cosmic rays (UHECR) which is a cosmic ray that has energy greater than 1 EeV, are not so recent anymore, and yet there is still much to learn about them [1].

UHECR undergoes a hardening in the energy spectrum called the ankle [2]. Above this energy, the flux has long been the hypothesis that it is primarily of extragalactic origin [3] which was also supported by the recent discovery of a dipole anisotropy in the arrival directions of UHECR with energies just above the ankle [4]. Another indication of the extragalactic origin of UHECRs is the flux suppression at around 40 EeV where propagation should become less diffusive [4].

The mass composition at energies above 40 EeV is best described as a mixture of light, intermediate, and high-mass nuclei, such as protons, helium, nitrogen, and iron nuclei [5]. Since we are observing mix composition of the mentioned nuclei, this gives a indication that some proprieties of the particles are modified throughout their journey. Examples of UHECR properties that are modified are. The arrival direction, the chemical composition and the energy of the particles. This can be caused by many factors, such as deflections in the extragalactic and galactic magnetic fields or more severe energy loss effects that depend primarily on the mass and charge [6]. For that reason, it is important, if not vital, to study simultaneously the effect of propagation of cosmic rays from their sources to Earth together with measurements of UHECR on Earth by large-area observatories.

In this diploma thesis, we use an open-source simulation framework for the propagation of cosmic rays called CRPropa 3 [7]. This in combination with real Monte Carlo simulations of the detector response at the Pierre Auger Observatory is used to investigate changes in mass composition anisotropy in the arrival directions of UHECR. X_{max} (depth of the shower maximum) is sensitive to mass and, therefore, allows us to analyse this behaviour. In addition to simulations, X_{max} can be well measured by modern observatories, which allows for a comparison between the observed and simulated mass anisotropy, which was observed by the Pierre Auger Observatory [8] and recently updated [9].

The first part of this diploma thesis will introduce a brief historical introduction together with some basic properties of cosmic rays. Then Chapter 2 will proceed with the propagation of UHECR in the universe, their energy losses, and their interactions with background radiation. We also describe the model of the galactic magnetic field that is used and how it affects UHECR. In Chapter 3, the Pierre

Auger Observatory is briefly described together with some observation techniques used. Chapter 4 is dedicated to the motivations and a closer look at the results observed at Pierre Auger Observatory, from which the idea for this thesis came. Chapter 5 includes some characteristics of simulation frameworks dedicated to the propagation of cosmic rays in the universe, together with other tailored parameters to achieve real conditions. Last but not least, the results for each of the analyses done and its findings are closely discussed, which is then followed by a conclusion.

Chapter 1

Ultra-High Energy Cosmic Rays

The discovery of cosmic rays serves as a prime example of how seemingly random noise can in fact contain valuable information.

Since the early 1900s, cosmic rays have been a subject of intrigue and speculation. Victor Franz Hess was one of the first physicists to conduct a series of experiments from 1911 to 1913 to reveal the truth about ionisation that was always present. These experiments involved measuring ionisation levels at different altitudes using a hot air balloon together with an electroscope to record data. In contrast to the prevalent hypothesis of the time, Hess's measurements revealed that ionisation levels increased with elevation, indicating that the radiation was not of terrestrial origin but rather coming from outer space. This pivotal discovery marked the dawn of a new era of exploration of the nature and sources of cosmic rays [1].

Some time later physicist, Pierre Victor Auger, together with Rossi, Boethe, Schmeiser, and Kolhorster, made a critical discovery by identifying extensive air showers of secondary particles from cosmic rays. This discovery played a fundamental role in the establishment of the Pierre Auger Observatory [10] as outlined in Chapter 3. It is established that cosmic rays are charged particles, with protons representing the majority of cosmic rays. For cosmic rays above energy 10^{18} eV its (approximately 86%), followed by helium nuclei (approximately 11%), and nuclei of heavier elements up to iron [11]. Such distribution belongs to particles often originating outside the Solar System and are called primary particles of cosmic rays. However these fractions vary highly over the energy range of cosmic rays.

There also exist a subset of cosmic rays, which then represent highly energetic particles whose origin is believed to lie outside our galaxy. These are known for their high energies ranging from 10^{18} eV to 10^{20} eV or higher and are called ultra-high energy cosmic rays (UHECRs). Today, the origin of UHECR remains one of the primary enigmas in astroparticle physics. Although it is believed that they come from extragalactic sources, the particular sources and mechanisms of their acceleration are still not fully understood.

Investigating UHECRs poses several challenges due to their rarity. As they are extremely rare, with only a few arriving to Earth per square kilometre per year. To study these particles, mainly ground-based observations are used; such as the Pierre

Auger Observatory, more about this observatory can be found in Chapter 3.

Despite the amount of time since the discovery of UHECRs, a number of critical questions still remain unanswered, such as the nature of the primary cosmic rays, their most powerful energies, their potential sources and acceleration, the cut-off in their energy spectrum at the highest energies, which can be caused either by their interactions with cosmic microwave background or by reaching the maximal accelerations. Various theories about origin of UHECR have been proposed, which could include topics such as active galactic nuclei or gamma-ray bursts.

In this Chapter, we discuss the properties of cosmic rays, with a particular focus on UHECRs. The topics covered will include the energy spectrum and mass composition, as well as the relation to X_{max}.

1.1 Energy spectrum

The energy spectrum of cosmic rays has a wide range of energies. It can be typically described as a power law, which means that the number of cosmic rays with energy E decreases as $\frac{dN}{dE} \approx E^{\gamma}$, where γ is a constant called the spectral index. This power-law behaviour is observed across many orders of magnitude in energy, from low as 10^9 eV up to 10^{20} eV.

Thus, the energy spectrum below an energy of $E \approx 4 \cdot 10^{15}$ eV can be approximated with a spectral index of $\gamma \simeq -2.7$. However, the spectrum undergoes significant changes in its behaviour at various energies. A steepening of the spectrum known as the "knee" occurs at an energy of $E \approx 10^{15.6}$ eV, where the spectral index changes to $\gamma \simeq -3.1$. Another steepening, called the "second knee," is observed around an energy of $\approx 10^{17}$ eV [12]. The spectrum hardens at $E \approx 5 \cdot 10^{18}$ eV, which is known as the "ankle," with a corresponding spectral index $\gamma \approx -2.5$ [13]. After such energy we can observe a recently identified feature called the "instep" with $\gamma \approx -3.05$. The spectrum ultimately reaches a cutoff at the highest energies of $\approx 4 \cdot 10^{19}$ eV with spectral index changing to $\gamma \approx -5.1$ [14] see Figure 1.1 for full overview. These variations reflect the mechanisms underlying the acceleration and generation of cosmic-ray particles for a given energy where factors such as particle rigidity[1] play an important role.

Figure 1.2 shows that the contribution of light elements to the spectrum is largely dominant from the knee up to the ankle region after which we see the heavier elements gradually take over. As proposed by Peters [15], there is maximal energy to which protons can be accelerated that also applies for different particles. Different particles can be accelerated to different maximal energies. This mechanism is then fully depending on the particle rigidity. This causes protons to be cutoff first, which then follows by the other particles due to the apparent lack of sources in the Galaxy

[1] Is a measure of a charged particle's resistance to bending due to magnetic fields defined as R = pc/q, where p is particle momentum, c speed of light, q is charge. Higher-rigidity particles are less affected by magnetic fields and its direction is less effected as lower-rigidity particles direction are more effected by the field.

that could be capable of accelerating rigours particles. Therefore protons are wash out from the galaxy. This statement holds true up to the ankle at which the lighter particles from extragalactic sources starts to introduce themselves back, this once again can be seen in Figure 1.2.

The cutoff at the end of the energy spectrum was predicted by Greisen [16], Zatsepin, and Kuzmin [17]. They established a theoretical upper limit for the energy of protons and iron nuclei emanating from distant sources, which corresponds to the very end of the energy spectrum. This maximum energy of the extragalactic proton results from photopion production in interactions with cosmic microwave background (CMB)[2]. Hence, the point where the spectrum falls is sometimes known as a GZK cutoff whose energy value corresponds to about $E \approx 10^{19.7}$ eV (for protons). This can be observed in the measurements done by the Pierre Auger Observatory and the Telescope Array, who managed to demonstrate this steep falling of the energy spectrum above $\approx 10^{19.7}$ eV [18].

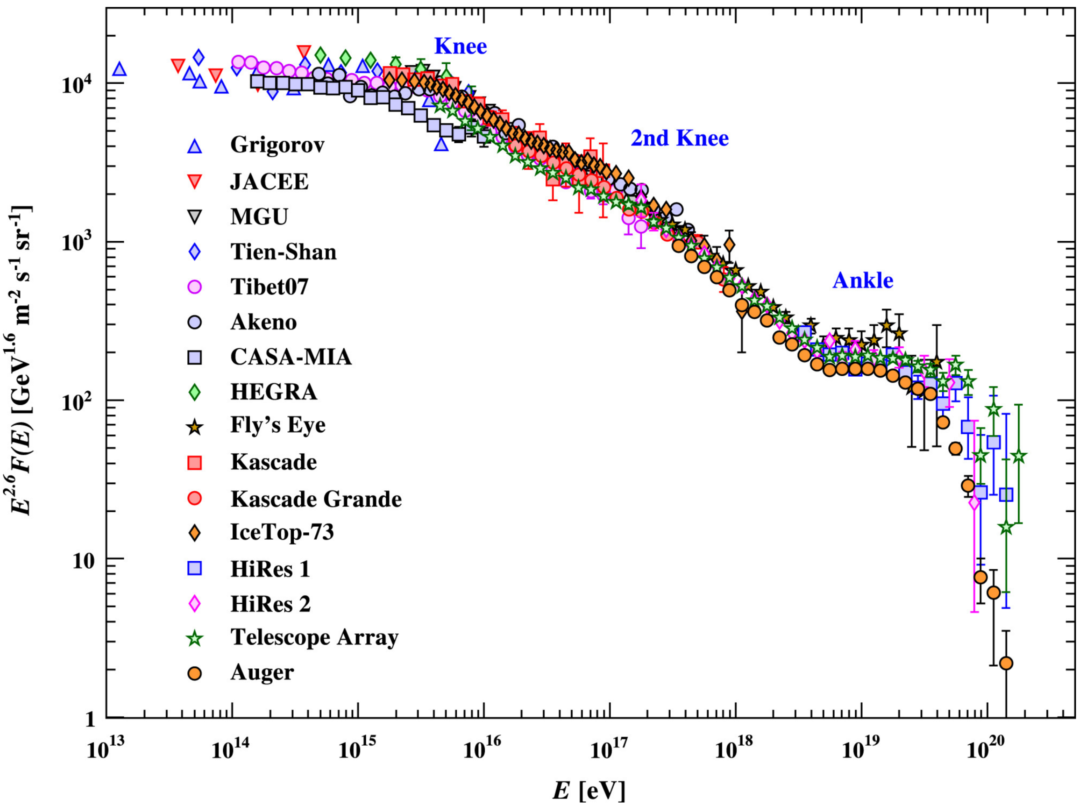

Figure 1.1: All-particle energy spectrum of cosmic rays. Note that the flux is scaled by $E^{2.6}$ [19].

[2]This radiation is a remnant from an early stage of the Universe, called the recombination, when the Universe became transparent to photons.

1.2 Mass Composition

The mass composition of cosmic rays detected at Earth varies with energy due to several factors. These include their sources, the distances they travel, and the magnetic field of the galaxy. The latter can lead to the trapping or acceleration of particles, a phenomenon also referred to as magnetic confinement. These factors can result in the dominance of certain nuclei over others at specific energies, which is important for understanding the physics behind the origin and propagation of cosmic rays. However, it is difficult to directly measure the mass composition of cosmic rays, as we can only detect the secondary particles produced in cosmic-ray showers from which the mass and energy of the primary particles can be deduced by closely analysing the properties of their secondary shower cascade.

The development of the corresponding electromagnetic and hadronic cascade [20] also characterised more accurately as slant depth X, is obtained by integrating the air density along the direction of arrival of the air shower through the curved atmosphere, as in

$$X(z) = \int_{z}^{\infty} \rho(\vec{r}(z'))dz', \tag{1.1}$$

"where $\rho(r(z))$ is the density of air at a point with longitudinal coordinate z along the shower axis" [21]. The specific depth at which the energy deposit reaches its maximum is called the depth of shower maximum, X_{max}. This is important because it is proportional to the logarithm of the mass "A" where A refers to the nuclear mass of the primary particle; however, it is important to realise that due to the fluctuation of hadronic interaction in the cascade the primary mass cannot be measured on event-by-event basis. The only way this can be approached is statistically. One approach is to use event weighting, where each selected shower is weighted according to the acceptance corresponding to the position of the shower maximum. This method compensates for the under representation of the distribution in certain regions by assigning weights to the showers. Another method is the $\Lambda\eta$ method, which subdivides the measured distribution into three regions: the central part with a constant acceptance, and the shallow and deep regions where the relative acceptance departs from unity. The true distribution of deep showers can be described by an exponential function, and the first two moments of the distribution can be calculated using this method. This, however, introduces numerous uncertainties, a detailed explanation can be found in [21]. However for the purposes of this diploma thesis, it suffices to mention that the final uncertainty of X_{max} smearing that is measured at Pierre Auger Observatory is 20 g/cm^2 [21].

X_{max} can provide important information about the mass and energy of the primary UHECR [21]. Its reconstruction is typically achieved by analysing the signals acquired from fluorescence detectors in conjunction with surface detectors which both are type of detectors used at Pierre Auger Observatory, more in dept discussion will be addressed in Chapter 3.

Figure 1.3 gives us a visual representation how heavier primary particles will produce shallower showers meaning it will have lower $X_{\max}$ value and also narrower $\sigma(X_{\max})$ than lighter particles, which on the contrary will produce deeper $X_{\max}$ values and also wider $\sigma(X_{\max})$.

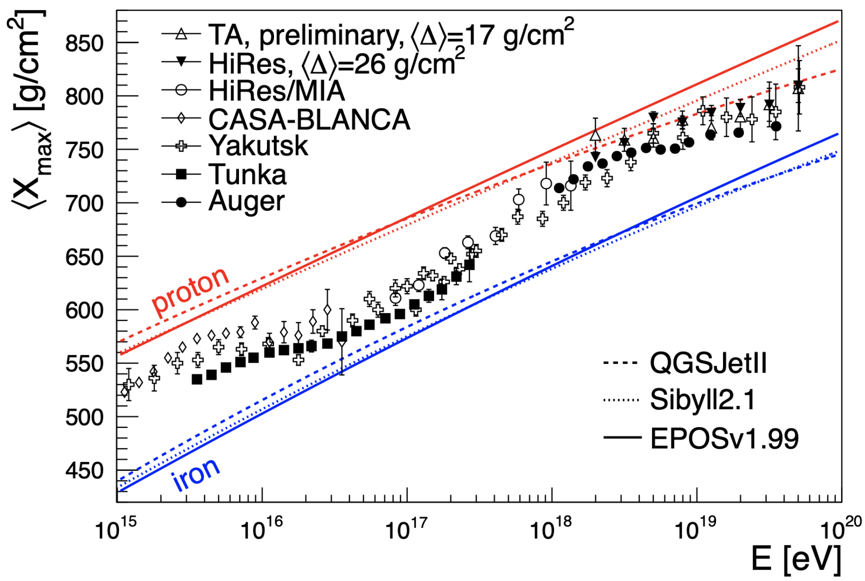

Figure 1.2: Measurements of the mean $X_{\max}$ with respect to energy from multiple experiments compared to QGSJet II, Sibyl II and EPOSv1.99 which are predictions of hadronic and electromagnetic simulations [10].

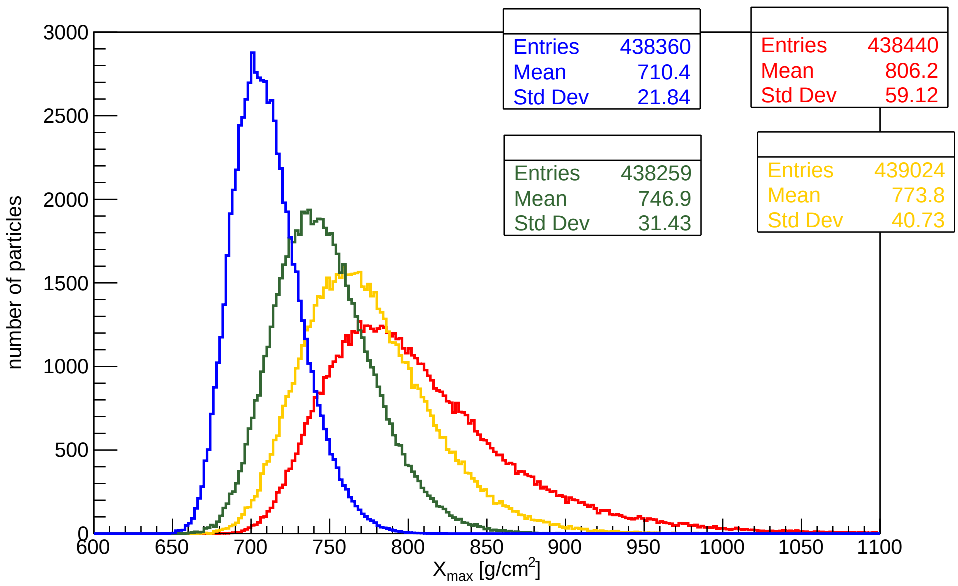

Figure 1.3: Figure which shows a distribution of shower maxima for different primary particles at energy $10^{18.8}eV$. It was obtained using simulated particles done in CR-Propa 3 software with applied corrections to mimic what is observed at Pierre Auger Observatory. Red (Proton), orange (Helium), green (Nitrogen), and blue (Iron).

Chapter 2

Propagation of Ultra-High Energy Cosmic Rays

The propagation of UHECRs in the universe is a complex and dynamic process that involves a range of physical phenomena. During their voyage, UHECRs interact with the CMB, which has a very small energy of around 10^{-3} eV [22]. Additionally, UHECRs can also interact with optical and infrared backgrounds as well as radio waves. These interactions can cause energy losses and changes in their chemical composition. Another important factor affecting the propagation of UHECRs is the presence of magnetic fields in both the galactic and extragalactic medium. These magnetic fields can deflect the trajectories of UHECRs, resulting in a diffusion-like behavior. As a result, the arrival directions of UHECRs might not directly indicate their original sources. Understanding these collective effects of the magnetic fields and background interactions and how they affect the UHECR propagation is essential for interpreting their observations.

In this Chapter, we will briefly discuss some energy losses that are relevant to the propagation of UHECRs, but we note that the focus of this diploma thesis is on their propagation within the Galaxy, where these losses can be neglected due to their relatively short distances [23]. Furthermore, we will provide an overview of galactic magnetic fields (GMF) and extragalactic magnetic fields (EGMFs) [24], with a greater emphasis on the GMF.

2.1 Energy Losses

2.1.1 *Photo-pion production*

One of the most significant particle energy losses is through the production of pions when the UHECR interact with the ambient photon background also called CMB or other photon backgrounds, such as the cosmic infrared background or the cosmic optical background. For head-on collision of nucleon with photon described as

$$N + \gamma \rightarrow N' + \pi, \tag{2.1}$$

with energy threshold

$$E^{N,\pi}_{thres} = \frac{m_\pi(m_N + \frac{1}{2}m_\pi)}{2\epsilon} \approx 6.8 \cdot 10^{19}\left(\frac{\epsilon}{10^{-3}eV}\right)^{-1} \text{eV}, \tag{2.2}$$

where the m_π and m_N are the masses of the pion and nucleon, respectively, and ϵ is the average energy of background photons [24].

Due to the extreme inelasticity of the process and the density of CMB photons, it was understood in the 1960s that the cosmos is opaque for ultra-high energy particles, resulting in GZK flux suppression. An example of such production is given by

$$p + \gamma \rightarrow \Delta^+ \Longrightarrow \begin{cases} n + \pi^+ & \text{with branching ratio } 1/3 \\ p + \pi^0 & \text{with branching ratio } 2/3 \end{cases}, \tag{2.3}$$

where in fact, they are the main channel for the production of ultra-high-energy secondary photons and neutrinos by hadronic cosmic rays [24].

2.1.2 *Pair production*

Another important process that contributes to energy losses is when a UHECR interacts with a photon from the CMB or other photon backgrounds, resulting in the creation of an electron-positron pair.

The energy threshold for this reaction is

$$E^{\pm}_{thres} = \frac{m_e(m_X + m_e)}{\epsilon} \approx 4.8 \cdot 10^{17} A(\frac{\epsilon}{10^{-3}eV})^{-1}\text{eV} \tag{2.4}$$

where $\mathrm{m_e}$ and $\mathrm{m_x}$ are the masses of the electron/positron and of nucleus X, respectively, and ϵ represent the energy of the background photon [24]. Due to its low threshold, this process is typically treated as a continuous energy loss process [24].

2.1.3 *Photodisintegration*

Photodisintegration of nuclei is another common process in which an atomic nucleus absorbs a photon, causing it to enter an excited state before disintegrating into two or more particles. The dominant photodisintegration processes vary, depending on the energy absorbed from the photons in the rest frame of the nuclei [24]. These energy losses can be described as

$$\left.\frac{1}{E}\frac{dE}{dt}\right|_{eff} = \frac{1}{A}\frac{dA}{dt}\sum_{i}\frac{i}{A}R_{A,i}(E), \tag{2.5}$$

where $R_{A,i}$ is the rate of emission of i nucleons from a nucleus of mass A [24]. This process not only alters the particle's energy but also reduces its atomic number, resulting in the creation of lighter particles.

2.1.4 *Adiabatic fractional energy loss*

Adiabatic fractional energy losses also known as cosmological redshift. Is another energy-loss process that dominates at low energies. It can be described as

$$-\frac{1}{E}\left(\frac{dE}{dt}\right)_{adiabatic} = H_0, \tag{2.6}$$

where H_0 is the Hubble constant [24].

In addition to the energy-loss mechanisms mentioned above, synchrotron radiation can also cause UHECRs to lose energy as they move through magnetic fields. This process occurs when charged UHECRs are deflected by magnetic fields, leading to the emission of electromagnetic radiation. However, compared to other processes, synchrotron radiation is a less significant mechanism of energy loss for UHECRs [24].

In general, these energy-loss mechanisms can significantly alter the original energy, direction, and chemical composition of UHECRs by the time they reach Earth. The complex interplay between these different mechanisms, combined with the uncertainties in the sources and propagation of UHECRs, makes the study of UHECRs a challenging field of research.

2.2 Magnetic Fields in the Universe

Magnetic fields are ubiquitous in the universe, and they play an essential role in various astrophysical processes, including the propagation of cosmic rays. Since cosmic rays are charged particles, they are subject to magnetic fields such that they are deflected by the Lorentz force.

Larmor radius r_L, which describes the radius of the circular path of a charged particle in a magnetic field, can be calculated by taking into account the particle's charge Z, energy E, and the strength of the magnetic field B. The formula for the Larmor radius is given as

$$\left(\frac{r_L}{\text{pc}}\right) = 1.1\left(\frac{E}{\text{PeV}}\right)\left(\frac{\mu G}{B}\right)\frac{1}{Z}. \tag{2.7}$$

There exist GMFs and EGMFs. Although the strength of GMF can be estimated from multiple measurements, the origin and strength of EGMF are not well understood, and its predictions vary considerably [24, 25].

2.2.1 Galactic Magnetic Field

The complex magnetic field present in the Milky Way is not exclusive to our Galaxy and can also be found in the interstellar and intercluster mediums, extending beyond the Galactic disks. These magnetic fields play a crucial role in various astrophysical phenomena, including guiding the motion of cosmic rays and shaping the formation and evolution of stars [26]. Moreover, the magnetic field contributes to the total pressure in the Galaxy [27].

The origin of GMF is still not fully understood, but it is believed to be related to the dynamo effect, which generates magnetic fields through the motion of charged particles in a rotating conducting fluid [27]. In the case of the Milky Way, which is a spiral galaxy, it is believed that the large-scale magnetic fields observed are amplified and maintained by the dynamo effect, which is thought to be driven by the combined action of differential rotation and helical turbulence [26].

In contrast, slowly rotating systems, such as elliptical galaxies and clusters, exhibit a distinct coherence scale that is smaller than the overall size of the system [25]. This suggests that these magnetic fields could be generated by a more chaotic local, turbulent dynamo where, in the absence of rapid rotation, the field does not organise on large scales. In itself, the dynamo paradigm must be considered incomplete, since it does not explain the origin of the initial fields that act as seeds for subsequent dynamo action.

The strength of GMF depends strongly on the type of the Galaxy, which implies whether the Galaxy has active dynamos (and thus large-scale magnetic fields) or not and since the probability of containing a large-scale magnetic field depends on the mass of the Galaxy, meaning that the mass of a Galaxy is also a factor, see [28]. For spiral galaxies the total magnetic field is about 10 μG, and then for the same galaxies, but with high star formation rates, it is about (20 - 30) μG. The strongest magnetic fields can then have magnitudes from 50 up to 300 μG, for example Messier 82. There are several ways to measure and quantify the strength of GMF.

Synchrotron Radiation: This is one of the most widely used methods for measuring the GMF in objects ranging from pulsars to superclusters. Synchrotron radiation is produced by high-energy electrons spiraling around magnetic field lines, and the intensity and polarisation of the radiation can be used to map the strength and structure of the magnetic field [25, 28].

Faraday Rotation: This method involves measuring the rotation of the plane of polarisation of the linearly polarised wave as it passes through the magnetic field. The amount of rotation depends on the difference in phase velocities of the right-circularly and left-circularly polarised waves. The change in the polarised angle which refers to the orientation of the plane perpendicular to the direction of a propagating electromagnetic wave, is linearly proportional to the square of wavelength

$$\varphi = \varphi_0 + (RM)\lambda^2, \tag{2.8}$$

where λ is the wavelength of the radiation, φ_0 is the initial polarization angle and RM is the rotation measure that can be obtained from

$$RM = \frac{e^3}{2\pi m_e^2 c^4} \int_0^{l_s} n_e(l) B_{\parallel}(l) dl, \tag{2.9}$$

where $B_{\parallel}$ is the parallel component of the magnetic field. As l goes from the observer to the source and m_e is the mass of an electron, $n_e(l)$ being the density of thermal electrons along the line of sight from the source [25].

Zeeman Effect: This method involves measuring the splitting of spectral lines which has normally levels of an atom that are independent of any direction of its angular momentum vectors. This degeneracy is lifted in the presence of a magnetic field by introducing a particular direction into the system, causing the very famous Zeeman splitting. It is the most direct method available for observing magnetic fields since once the difference in energies ΔE is measured, B can be determined, providing a measure of the strength of the magnetic field in a given region of the Galaxy [25, 28].

Gamma-Ray Observations: Its a indirect measurement where Gamma-ray telescopes such as the Fermi Large Area Telescope (LAT). Measure the energy and direction of gamma rays coming from different regions of the sky. By analyzing the distribution and characteristics of the gamma rays, one can infer the presence and properties of cosmic rays and the magnetic field they interact with [29].

It is extremely difficult to accurately determine the true nature of the GMF, leading to the development of various GMF models where some models consider the magnetic effects of the galactic halo to be minor compared to the rest of the Galaxy, while others consider the halo to be a significant contributor to the overall magnetic field. In this study, the Jansson-Farrar 2012 (JF12) model is used [30], which is commonly used GMF model in the astroparticle community.

Jansson-Farrar GMF model

First introduced in 2012 by Jansson and Farrar [30]. This model is based on a combination of observational data and theoretical calculations and offers a comprehensive framework for understanding the GMF.

It is based on the assumption that the GMF can be decomposed into two components: a large-scale component, which represents the regular field across large features, and a smaller-scale turbulent component arising from objects like supernovae. By employing a Bayesian statistical approach and incorporating observational data from various sources, including Faraday rotation RM values from multiple sources to form RM-pixels[1], along with synchrotron emission data, will result in the JF12 model see Figure 2.1.

First, the **(large-scale)** regular component, which is assumed to be axisymmetric and toroidal in shape, is further decomposed into three separate components. Considered a disk component, which is predominantly located in the plane of the Galaxy and is responsible for the majority of the GMF's strength in this region, the disk component is modelled after the generalised form of the Brown model [31].

The second component is the halo component, which extends above and below the Galactic disk and is responsible for the GMF's strength in the halo region. Several forms of this field are considered, including the axisymmetric and bisymmetric spirals, but the purely toroidal model held the superior fit to the data.

The third component is the X-shaped component, which has a unique structure that is aligned with the X-shaped bulge of the Galaxy. The X-shaped component is modelled as axisymmetric and poloidal, i.e., without any azimuthal component (which is incorporated via the toroidal halo component). It is defined with random orientation and strength on small scales, but its relative magnitude is the same throughout the Galaxy [32].

The **(smaller-scale)** turbulent component is modeled as random field. This turbulent component is thought to arise from the amplification of small-scale magnetic fields by turbulence in the interstellar medium [32].

2.2.2 Extragalactic Magnetic Fields

Magnetic fields exist beyond the confines of individual galaxies. The principles underlying the measurement of EGMFs are similar to those used to study GMF. However, the task of studying EGMF is considerably more challenging due to the vast distances involved and the much larger space that needs to be explored. The most successful measure of EGMFs comes from the measurement of the Faraday rotation of the few Galaxy clusters, which were within some reasonable range. The strength of magnetic field in Galaxy clusters, with the strongest EGMFs observed reporting strengths of up to several nanogauss around the range of 10 nG [33]. As its visible, this magnitude in comparison to GMF is much weaker.

The origin of EGMF is a topic of active research. Several theories have been proposed to explain the origin and evolution of these fields, although none have yet been conclusively proven. Some of the most prominent theories are

Primordial magnetic fields which talks about the existence of magnetic fields in the early universe, which were generated by various processes such as cosmic

[1] This process yields a data structure analogous to the synchrotron emission dataset.

inflation or phase transitions. These fields were subsequently amplified by gravitational collapse and other processes during the formation of structures, leading to the EGMF we observe today [34].

Exotic particles and interactions which propose the existence of new particles or interactions beyond the standard model, which could generate or modify magnetic fields in the universe. The idea behind this theory is that axion-like dark matter particles could decay into photons and produce magnetic fields in the extragalactic medium [35].

It is important to note that these studies are highly speculative and none have yet been conclusively proven.

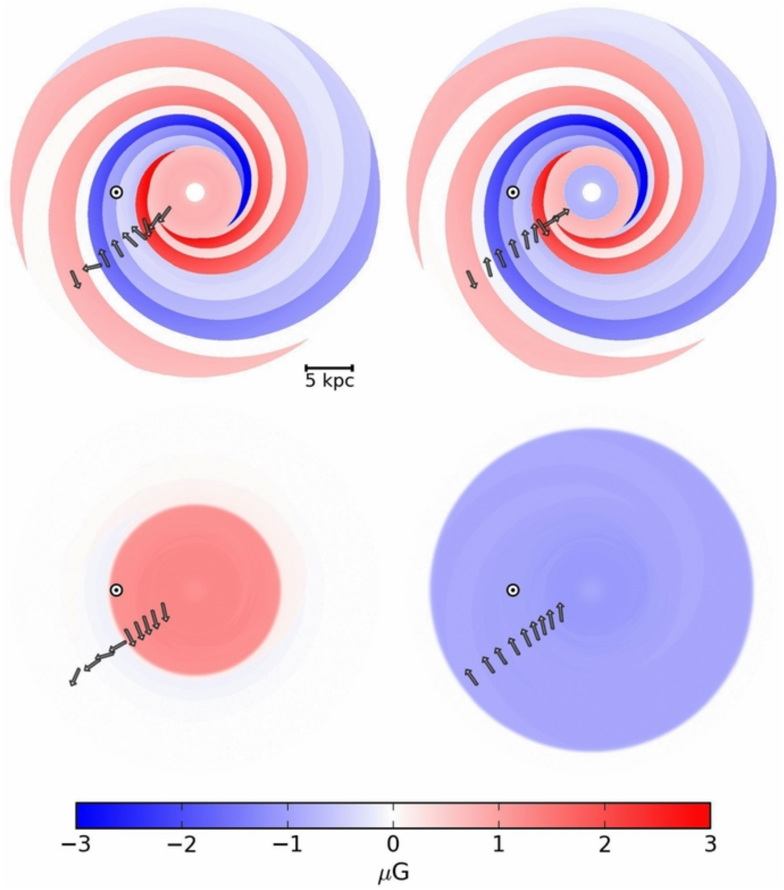

Figure 2.1: Top view of slices in the $x-y$ plane of the JF12 GMF mode model. Top row, from left, slices at z = 10 pc and z = -10 pc. Bottom row, slices at z = 1 kpc and z = -1 kpc, respectively. The color scheme shows the magnitude of the total regular field, with negative values of the azimuthal component is oriented clockwise. The location of the Solar system is marked with a circle [30].

Chapter 3

The Pierre Auger Observatory

The Pierre Auger Observatory is a state-of-the-art facility that is still undergoing updates for future experiments. It was initially "proposed during the International Cosmic Ray Conference in Dublin in 1991 by Jim Cronin of the University of Chicago and Alan Watson of the University of Leeds"[36]. They proposed this facility with a single goal. To investigate and understood cosmic rays of the highest energies. It all came together through a unique partnership of 18 countries, which pushed toward first constructions back in 2000 and was finished in 2008; however, first data collection started during the construction in January 2004 with 154 active detector stations. The first physics results were then presented during the 2005 summer conference [36, 37].

For the construction, it was important to choose the right location with sufficient area to host such a large experiment, as it had become clear that only a very large array would yield high statistical power to cover almost complete sky, which is necessary for the observation of the highest-energy cosmic rays. On the basis of these conditions, the province of Mendoza, located in Argentina, was chosen. It provided a generally flat area for which the detectors would be located at altitudes between 1340 and 1610 m. This allows for the network of 1660 Surface Detectors (SD) placed in regular triangular patterns with a spacing of 1500 m with a total area of approximately 3000 km^2 resulting in overall sensitivity for cosmic rays above 10^{18} eV. There also exists a smaller array of SD stations positioned within the overall array with a smaller array separation of 750 m between each SD detector. It was one of the Pierre Augers Observatory updates called AMIGA (Auger Muon and Infilled Ground Array), which aimed to extend the sensitivity up to 10^{17} eV, which allowed for the detection of less energetic cosmic rays. This is then surrounded with four fluorescence detectors (FD), see Figure 3.1, which shows detector positions where each red dot represents one SD station and the FD stations then surround the perimeter of the whole array, namely; Los Leones, Los Morados, Loma Amarilla, and Coihueco, together with its view direction visualised in green line. See Figure 3.2 for a visual representation of the FD and SD detectors.

The final design is a unique facility that uses two different types of detector to study cosmic-ray showers. The SD continuously records the particle densities as cosmic-ray showers hit the ground, and the FD measures the longitudinal development of the showers by detecting the amount of nitrogen fluorescence light produced along its path as a nearly calorimetric detector, allowing precise measurements of energy. SD offers an almost 100% duty cycle, while FD can only operate on dark and moonless nights which as a consequence has a duty cycle of around 15%.

An essential feature of Pierre Auger is its hybrid design. Observing showers simultaneously using two different but complementary techniques and combining them with respect to theirs energy, allows for a precise determination of the position of a shower axis in the atmosphere with an accuracy better than that that could be achieved independently with either the SD or FD [36].

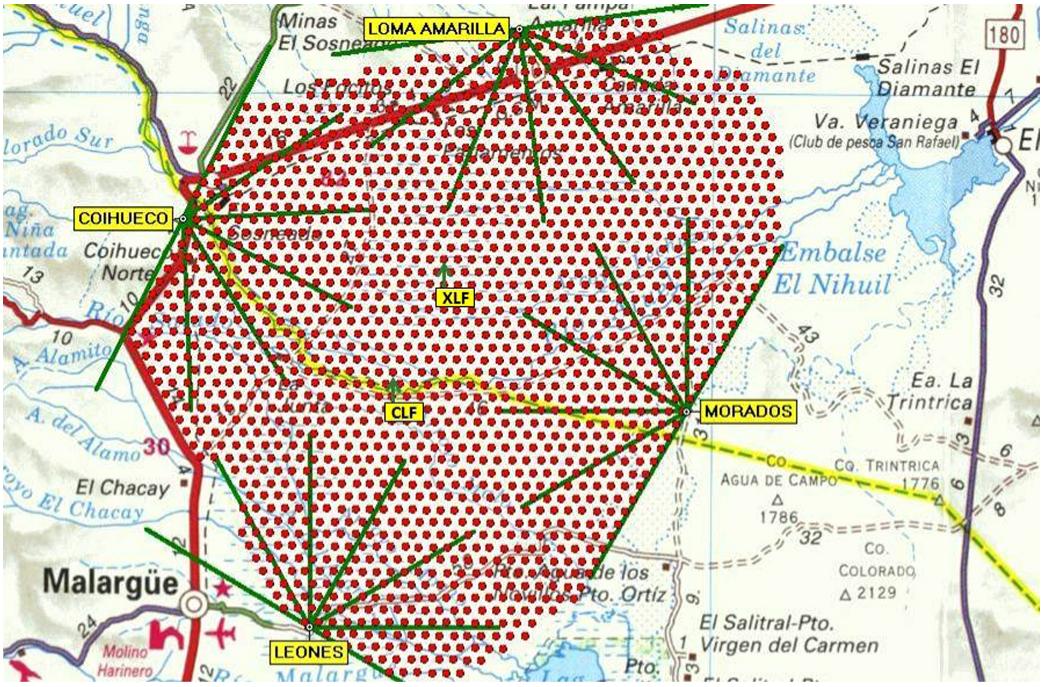

Figure 3.1: Detector layout of the Pierre Auger Observatory. Each red dot represents one SD station. The four FD sites, labelled yellow, are also shown with an indicated field of view (green) for each of the individual telescopes [36].

Figure 3.2: Los Leones fluorescence detector enclosure (top) and surface detector station (bottom) [36].

3.1 Surface Detectors

Surface detectors, specifically water Cherenkov detectors, consist of fully autonomous cylindrical tanks, measuring 3.6 metres in diameter and 1.6 metres in height. A schematic representation of the SD detector is shown in Figure 3.3. The inner surface of these tanks is designed to be highly reflective, and they are sealed with a specialised liner. This design allows the tanks to hold up to 12,000 litres of ultrapure water, ensuring clarity and preventing bacterial growth which could otherwise compromise water clarity. Inside these tanks, are three Photonis XP1805/D1 photomultiplier tubes (PMTs), each 9 inches in diameter, are strategically situated in such a way to minimise the impact of the geomagnetic field. Their orientation is aligned with the azimuth of Earth's magnetic field to capture Cherenkov light [36].

When relativistic charged particles or high-energy photons move through the water at a speed greater than the speed of light in that medium, it polarises the nearby atoms, which generate Cherenkov light that is subsequently registered as a signal by the photomultipliers. This signal is quantified in units of Vertical Equivalent Muon (VEM)[1]. However, prior to any energy reconstruction or additional calculations, the SD requires calibration to accurately measure the value of 1 VEM. During shower reconstruction, the signal recorded by the tanks, is converted into units of VEM, is

[1]A signal produced by a muon traversing the tank on a vertical trajectory.

then used to fit the total shower energy and arrival direction which are determined using a lateral distribution function (LDF). This is then used to model the lateral distribution of the signals on the ground.

Each SD station is also equipped with a GPS receiver and data acquisition system used to record the detection time in each SD, which is then synchronised across each SD station to determine where the shower was detected first. In addition, an accompanying radio transceiver and power controller are included, as well as a control function whose purpose is to monitor the performance and reliability of the SD array. It ensures that the SD is functioning properly and provides data quality monitoring that allows remote operation [36].

These SD stations not only exhibit exceptional geometry and reliability, which include minimal maintenance requirements, and cost-effectiveness. Such durable solar powered equipment with a duty cycle of nearly 100% is ideally suited for the prevailing environmental conditions [36].

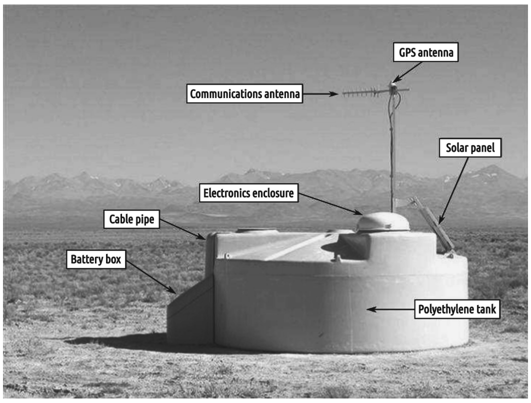

Figure 3.3: A schematic view of a surface detector station in the field, showing its main components [36].

3.2 Fluorescence Detectors

In the observatory there is total of 24 FD telescopes from four distinct sites to cover the space above the array of SD. Each FD station houses six independent telescopes located within clean, climate-controlled buildings. These telescopes have a field of view of (30 x 30)° in azimuth and elevation, providing a cumulative coverage of 180 ° in azimuth [36].

The telescope design is based on Schmidt optics, which reduce coma aberration, while an annular lens further eliminates it and corrects for spherical aberration. The schematics of such a telescope are illustrated in Figure 3.4. Fluorescence light, emitted by an air shower, enters through a circular diaphragm with a radius of 1.1 metres [36]. Positioned behind a Schott MUG-6 filter glass window, this diaphragm serves as a UV spectrum filter, allowing between 50 and 80 % of UV light to pass through. It is crucial to note that these percentages are based on light wavelengths ranging from 310 to 390 nm. The minimal UV losses yield a substantial reduction in other background light fluxes, thereby enhancing the signal-to-noise ratio. The diminished light subsequently falls onto a hexagonal or rectangular segmented spherical mirror with a radius of 3,400 mm and is then focused onto a camera equipped with 440 photomultipliers [38].

As previously stated, FD stations have a duty cycle of approximately 15% due to not being able to operate in daylight, in addition to conditions such as bad weather or high flux from moonlight which also reduce this duty cycle. To prevent potential damage to the detectors, the stations are equipped with shutters that close during daylight hours and automatically shut at night when the wind speeds increase or rainfall is detected. Additionally, a fail-safe curtain is mounted in the background. All FD telescopes are then remotely operated by shift personnel from the central campus.

As mentioned, the FD stations measure the longitudinal profile, which is utilised in conjunction with SD in hybrid reconstruction. Further details on this process are provided in the following section.

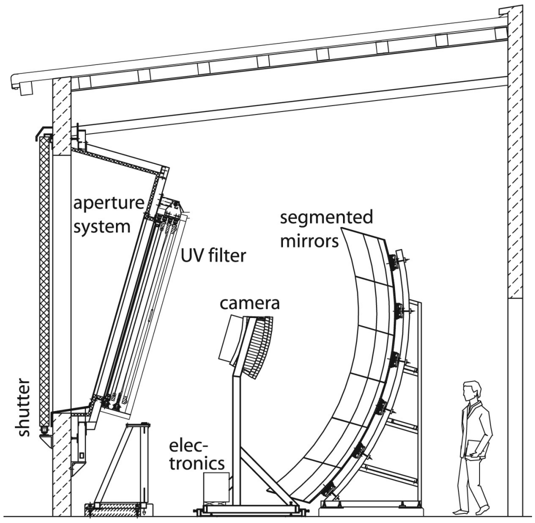

Figure 3.4: Schematic view of a fluorescence telescope with a description of its main components [36].

3.3 Hybrid Reconstruction

Key feature of the Pierre Auger Observatory is its hybrid design, which allows the measurement of properties of primary cosmic rays by using different techniques for which we have different varying systematic uncertainties. For the reconstruction, the data of both FD with additional timing information from the SD are exploited such that the amplitude and timing of the signals detected by each PMT in each telescope as well as additional timing information from the SD station with the highest signal, improve the directional precision. Such precise geometry of the hybrid event is the first step toward high-quality measurements of the longitudinal profile of the shower, which, in turn, yields the energy of the primary particle and the depth of maximum

X_{max} with statistical resolutions for a single site of approx 10% and 20 g/cm^2 for energy and X_{max}, respectively, at around 10^{19} eV [36, 39, 40].

An additional example of the synergy between the two techniques can be shown in a situation where showers arriving with zenith angles less than 60° will under normal conditions provide better exposure when only SD is involved. However, the surface array presents a challenge when trying to correlate the primary energy with a specific observable, such as the signal measured by the water Cherenkov detectors located 1,000m from the shower axis S(1000)[2], which can only be found using cascade simulations. This is a problem as this method is unreliable since the hadronic physics for such energies is unknown and, therefore impractical to assign systematic uncertainty. Here, using the hybrid system provides an alternative method which is essentially free from using simulations (the reason why not completely free is due to the small fraction approx. 10% that goes into neutrinos and high-energy muons that continue into the ground) [36].

[2]Total signal at a core distance of 1000 m.

Chapter 4

Physics Motivation for mass-dependent anisotropy studies

The primary motivation for this diploma thesis stems from the substantial contributions made by the Pierre Auger Observatory in advancing our understanding of the mass composition of cosmic rays that arrive on Earth.

In 2016, the observatory published a study [41] that provides a compelling evidence for a mixed mass composition of cosmic rays. This is particularly evident in the so called "ankle", a region that can be characterized by its change in the slope of the cosmic-ray spectrum. It is observed within the energy range of $\log(E/eV) = (18.5, 19.0)$, as shown in Figure 4.1.

The significance of the ankle region lies in its potential to provide insights into the composition of cosmic rays or it might mark the transition between galactic and extragalactic cosmic rays.

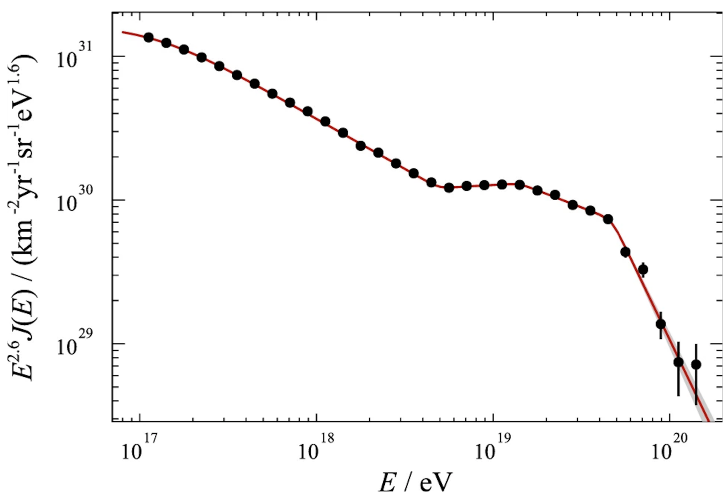

Figure 4.1: SD energy spectrum after combining individual measurements with the SD-750 and SD-1500 scaled by $E^{2.6}$. The fit using the proposed function labeled as (Eq. (9) in [42]) is overlaid in red along with the one-sigma error band in gray which represent statistical uncertainties [14].

The aforementioned article also discusses the measurement of the correlation between the depth of shower maximum ($X_{\rm max}$) and the signal in the water Cherenkov stations of air-showers. The results can be seen in Figure 4.2. A ranking coefficient r_G introduced by Gideon and Hollister [43] is used as a measure of the correlation between two variables. The ranking coefficient is chosen due to its invariant properties against any modifications that do not change the ranking order of the data (such as systematic shifts in the observable). The primary difference between this particular ranking coefficient and others lies in the fact that the actual rank values themselves are not used directly in the calculations, it uses the ranks to determine the correlation between two observable without relying on the specific values of the ranks, thereby establishing a unique approach, where the general statistical dependence between X^*_{max} and S^*_{38} is estimated by counting the difference in numbers of events with ranks deviating from the expectations for perfect correlation and anti-correlation [41].

In simulations, it is observed that pure cosmic-ray mass compositions typically yield a correlation coefficient r_G close to or greater than zero. Conversely, mixed mass compositions exhibit a negative correlation. Data from two independent detection techniques are used to mitigate systematic correlated detector bias. The first technique employs FD to measure $X_{\rm max}$, while the second uses $S(1000)$ which is notably sensitive to muons. Both $S(1000)$ and $X_{\rm max}$ are influenced by shower energy; additionally, $S(1000)$ is affected by the zenith angle. To standardize these variables, $S(1000)$ and $X_{\rm max}$ are scaled to a reference energy of 10 EeV and a zenith angle of 38°, resulting in scaled quantities denoted as $X^*_{\rm max}$ and S^*_{38} [41].

The resulting correlation mentioned in Figure 4.2 is $r_G = -0.125 \pm 0.024$ indicating that particles whose energies are within the ankle region consist of a mixed mass composition [41].

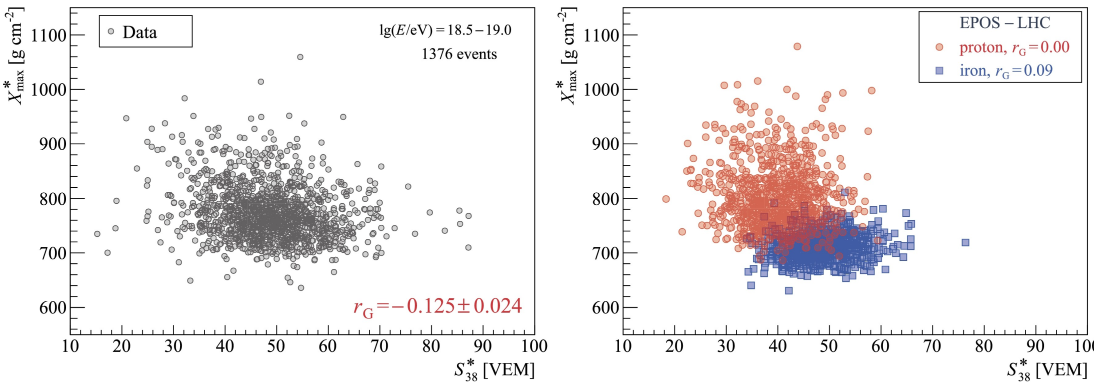

Figure 4.2: Left: measured distribution of $X_{\rm max}$ vs. ground signal S_{38}, both corrected for energy evolution, for $\log(E/eV)$ = 18.5 -19.0. Right: the same distribution for 1000 proton and 1000 iron nuclei showers simulated with [EPOS-LHC] [41].

In 2017, the Pierre Auger collaboration makes a significant discovery, unveiling a large-scale dipole anisotropy for cosmic rays with energies above 8 EeV. This is established with a significance of $> 6\sigma$ [4]. The study shows that only the dipole components orthogonal to Earth's rotation axis and along Earth's rotation axis are statistically significant. Furthermore, the dipole is positioned approximately -125° away from the Galactic Centre, as illustrated in Figure 4.3. This anisotropy suggests that these UHECR particles likely have extragalactic origins.

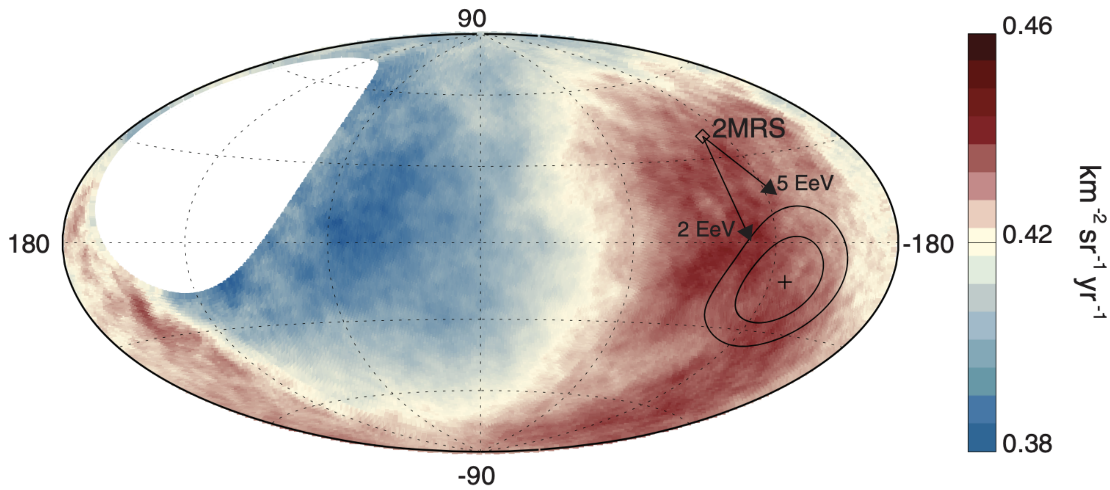

Figure 4.3: Cosmic-ray flux detected by the Pierre Auger Observatory above 8 EeV, shown in galactic coordinates and smoothed with a 45° top-hat function. The galactic Centre is at the origin. The cross mark represent the measured of dipole direction, and the contour represents the 68% and 95% confidence level regions. The dipole in the 2MRS galaxy distribution is indicated. Arrows show the expected deflection for the JF12 [30] GMF, as described in Chapter 2.2.1, for particles with $E/Z = 5$ or 2 EeV. Adapted from [4].

The following study by [8] proposes a hypothesis of anisotropic behavior along the Galactic plane for energies of $10^{18.7}$ eV. The measurement is analyzing fourteen years of data, shown in Figure 4.4. It is evident that the $\langle X_{\max} \rangle$ and $\sigma(X_{\max})$ for the on-plane region defined as particles within $\pm 30^{\circ}$ from the Galactic plane using galactic latitude, have a shallower mean mass of $(9.1 \pm 1.6)\,\mathrm{g/cm^2}$ and a narrower width of $(5.9 \pm 2.9)\,\mathrm{g/cm^2}$ compared to those from the off-plane region. The initial significance is 4.4σ when applying the in-FidFoV cut, which refers to events within the fiducial field-of-view (FidFoV)[1].

[1] FidFoV refers to the region of observation in a experiment where the data is considered reliable and accurate. It minimize the influence of the effective field of view on the distribution of $X_{\max}$ of air showers. It is achieved by selecting specific geometries that have a large accessible field of view, in other words it constrains the FD detector volume to only event geometries where the expected range of $X_{\max}$ values would be visible in the FD. This will changes the natural FD $X_{\max}$ acceptance (gray) see Figure 4.5 to the one which is unbiased from ~600 to ~900 g/cm^2. This spans the typical range of observed event $X_{\max}$ values and ensures that the $X_{\max}$ distribution is not significantly distorted [21].

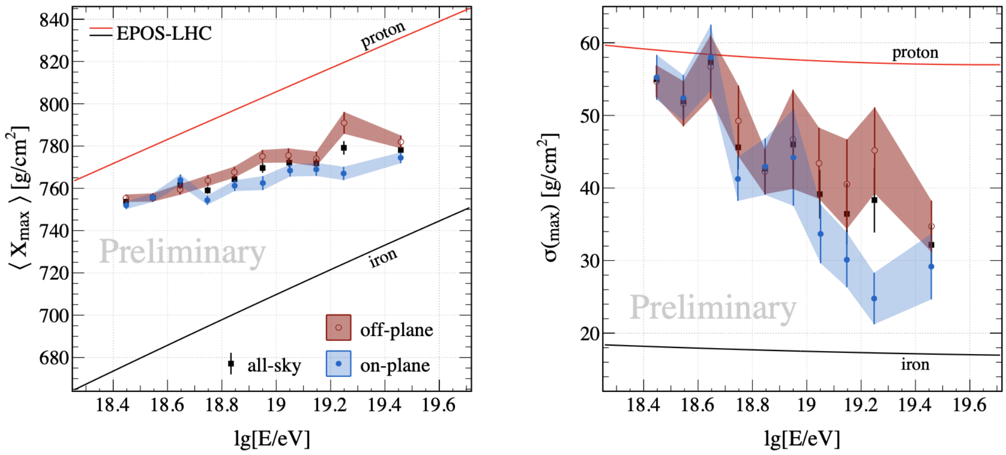

Figure 4.4: The $X_{\max}$ moments of the on-off-plane regions [8].

An update published in 2023 [9], corrects the difference in $\langle X_{\max}\rangle$ to approximately $5\,\mathrm{g/cm^2}$ with a confidence level of 2.2σ. This adjustment is made by considering showers falling out of the FidFoV, allowing for an additional dataset, termed as out-FidFoV cut events. These are events that fall outside the fiducial field-of-view. The primary distinction between the two datasets is that the in-FidFoV focuses on a specific region of the sky, while the out-FidFoV encompasses events from a broader area.

In the following Figure 4.6 we can then view the composition sky map of the relative mixes of cosmic rays above $10^{18.7}$ eV, which shows an indication of some differences between the planes.

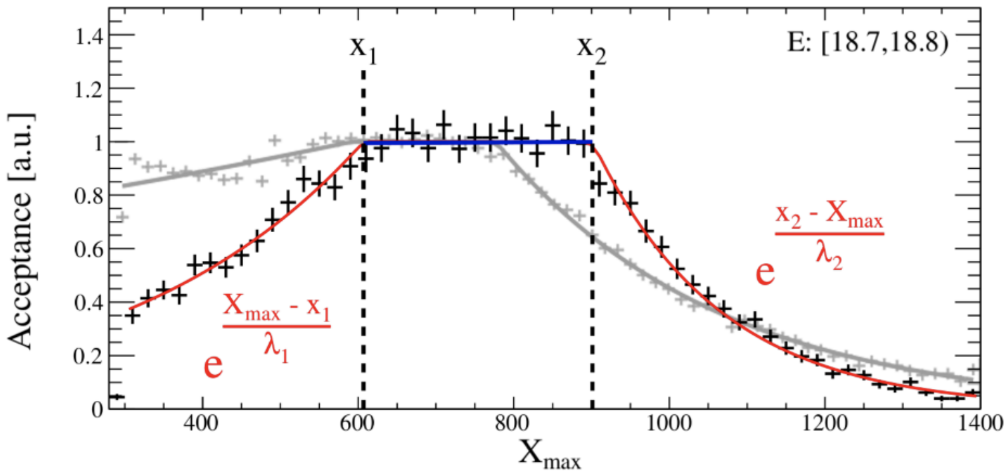

Figure 4.5: FD $X_{\max}$ acceptance before (gray) and after (black) FidFoV cuts. A 4-variable parameterization of the post-FidFoV acceptance is shown in red. The range of $X_{\max}$ values with unbiased sampling is shown in blue [9].

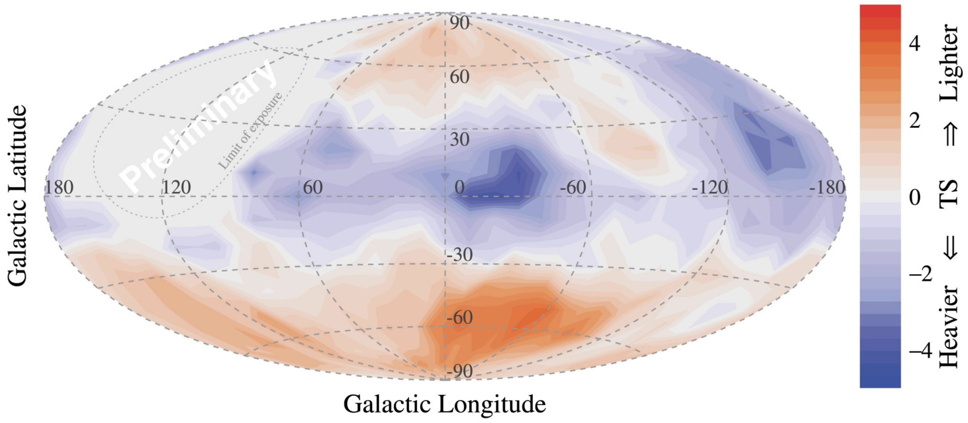

Figure 4.6: Sky map of comic-ray composition for E greater than $10^{18.7}$ eV [8]. Where the Z-axis is the test statistics of the the Anderson-Darling 2-samples homogeneity test [44].

There exist several approaches for this dipole observed phenomena that can result in not just the mass dependent anisotropy. To mentioned few, the study [45], investigates the implications of recent observations of anisotropies in UHECRs. It analyzes the large-scale anisotropies and composition features and discuss how these observations can provide insights into its origin. They utilize simulations to generate realistic UHECR sky maps for various scenarios. One of the scenarios is to test the difference in $X_{\max}$ distribution when comparing the on-off galactic plane. The result shows that the simulated sky maps do show differences between the regions on and off the galactic plane. In the analysis, there is an excess of event count ranging from approximately 1.5σ to 4σ in the on-plane region compared to the off-plane region. This indicates a difference in the composition of cosmic rays between these two regions. The differences in the values of $\langle X_{\max} \rangle$ and $\sigma(X_{\max})$ results to be approximately two times lower. However, it should be noted that the magnitude of the difference found in the simulated sky maps is much smaller than what has been reported in [8, 9].

Hence it is important to note that no other study reports the magnitude of the observed differences and it can be clearly said that such inconsistencies arises from our incomplete understanding of the UHECRs, as there could be various factors that we have to take into consideration when dealing with this unknown. Some of many possible causes can be the presence of another particle generator within the galaxy or inaccuracies in our GMF model, the existence of multiple dipoles, among others.

These inconsistencies serve as the driving force behind this diploma thesis, which aims to address questions related to the compositions and mixtures that could affect the GMF or dipole. In subsequent chapters, this diploma thesis attempts to replicate the initial findings of [8] or its updated version [9] within a simulated environment. Following this, it delve into additional analyses considering the position of the dipole and its impact on anisotropy. The main framework and approach for simulating particles for use in these analyses will be described, and the results for three different analyses will be presented.

Chapter 5

Cosmic ray simulations

In the following Chapter, a simulation setup for generating particles and various methods to match real observable conditions were introduced. The endpoint is to produce data that closely approximates real observable conditions.

5.1 Simulation of cosmic ray propagation

To simulate particles that also interact with GMF for multiple elements. An open source framework simulation called CRPropa 3 is used. It is a publicly available software written in C++ and can be imported as a Python 3 library. Its modular structure is shown in Figure 5.1 [7].

The initial setup involves modules such as the three-dimensional mode of CRPropa 3, which propagates particles in three dimensions. This is followed by the addition of magnetic fields for which CRPropa 3 offers both the GMF and EGMF, however since this project focuses on particles within the Galaxy. Therefore, only the GMF and its corresponding JF12 model (see Chapter: 2.2.1) is used. Due to the propagation in relatively short distances, one can neglect energy losses (see Chapter 2.1).

The observer is defined as a spherical source with a 20 kpc radius. This allows the use of CRPropa 3 in the so-called **Back-tracking**. It is a general method that considers the observer as a starting point and propagate particles isotropically away from this point-like source. Each particle is with opposite charge acting as antiparticle. In this case the particles are propagated towards the edge of the Galaxy. The advantage is the reduced computational time, as all particles are included in the final output. The validity of this approach can be demonstrated in the Appendix: B, where is compare to a forward-tracking method obtained by the author of [46]. Where the particle are generated at the edge of the galaxy and propagates then towards the observer. Both methods produce equivalent results. Therefore, the less time-consuming backtracking method is chosen to propagate 1,000,000 individual protons, helium, nitrogen, and iron nuclei through the GMF. The energy spectra follows a power law E^{-1} and span an energy range from 3.15 EeV to 100 EeV. The Python code used for the simulations can be found in the appendix: A.

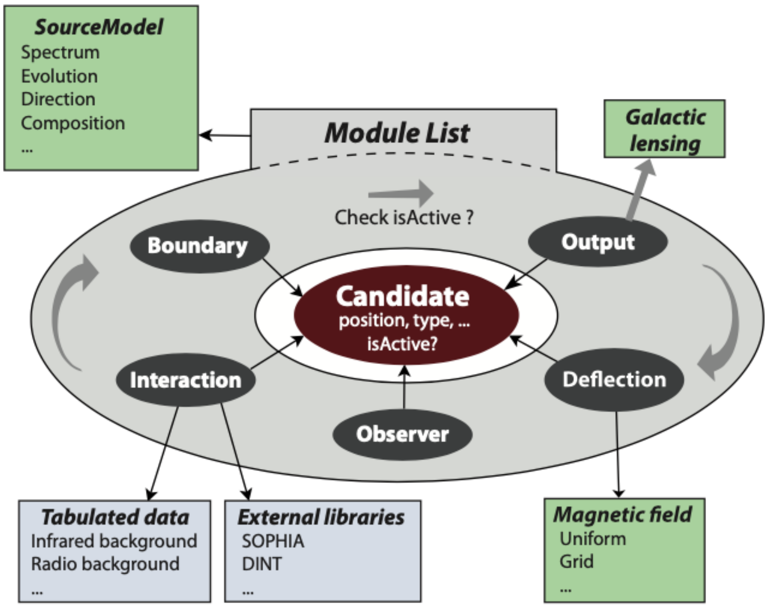

Figure 5.1: Illustration of the modular structure of CRPropa 3. Each module contained in the module list acts on the candidate class [7].

5.2 Estimation of relative FD exposure

Real Monte Carlo simulations [47] are used as a means to estimate the relative FD exposure. It is a tailored Monte Carlo approach that is designed to closely emulate realistic scenarios and incorporates details about the detectors to adjust the simulated data to match the real-life observations. To be more precise, the Offline v3r3p4-icrc2017-preprod-v3 which is a general purpose framework that allows collaborators to contribute algorithms and sequencing instructions to build a variety of applications [48]. It consists of three distinct hadronic interaction models, all of which are used, namely QGSJet II-04 [49], EPOS-LHC [50] (using CONEX 5.40) and Sibyll 2.3c [51] (CONEX 5.64) where CONEX is a hybrid simulation code that is suited for fast one-dimensional simulations of shower profiles [52]. The hadronic models cover a range of energies from 0.4 to 158 EeV. The simulated energies are then corrected to correspond to the observed energy spectrum [42] with the spectral index of the generated energy spectra being 1.75. This is similar to our simulations done in CRPropa 3. The simulated showers are then passed through series of high-quality selections for X_{max} analysis together with energy selection between 5 and 100 EeV. Only after this, the Monte Carlo simulated particles are plotted and used as a lookup map to estimate the relative FD exposure on arrival direction; see Figure 5.2.

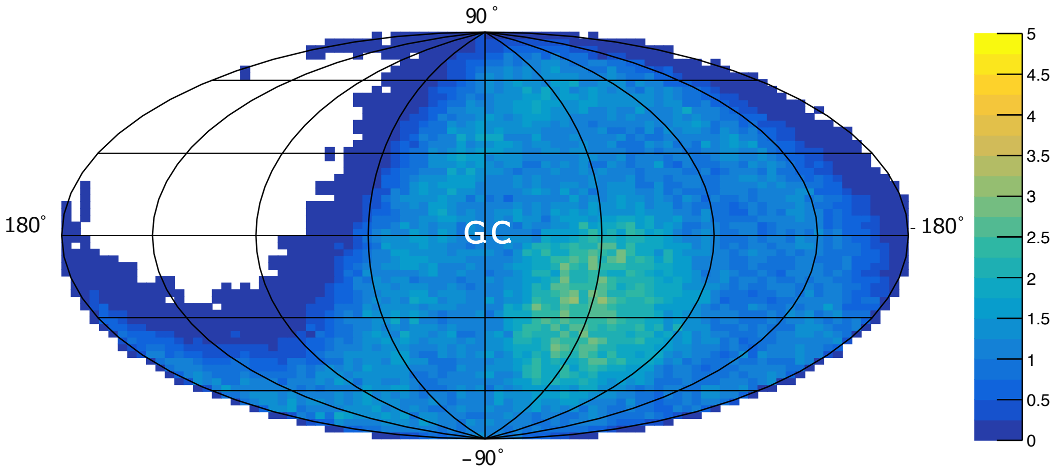

Figure 5.2: The estimation of relative exposure of FD of the Pierre Auger Observatory obtained from real MC simulations in galactic coordinates.

5.3 Correction factors

Since the simulated particles generated by CRPropa 3 are isotropic, to resemble real-world conditions observed at the Pierre Auger Observatory, multiple weights need to be applied. In this section of this chapter each of the applied weight is described.

Dipole: Further denoted as W_1 representing the first weight. It is calculated by the following equation:

$$W_1 = \mathrm{AP} \cdot \cos(\delta) + 1.0, \tag{5.1}$$

where "AP" is the amplitude of the dipole and δ represents the angular distance between the initial direction of the simulated particle and the direction of a dipole. It is defined as follows:

$$\delta = \arccos\left[\sin(\mathrm{b_D}) \cdot \sin(\mathrm{b_{In}}) + \cos(\mathrm{b_D}) \cdot \cos(\mathrm{b_{In}}) \cdot \cos(\mathrm{l_D} - \mathrm{l_{In}})\right], \tag{5.2}$$

where "$\mathrm{b_D}$" and "$\mathrm{l_D}$" represent the positional coordinates of the dipole in galactic coordinates. The other variables "$\mathrm{b_{In}}$" and "$\mathrm{l_{In}}$" denote the initial latitude and longitude of the simulated particle.

Relative FD exposure: Denoted as W_2, this represents the second weight that is obtained from the real MC simulations described in previous section of this chapter by, utilizing ROOT's [53] functions FindBin and GetBinContent, which are applied to the histogram shown in Figure 5.2.

Correction for Energy Spectrum: Denoted as W_3, this represents the third weight that corrects the spectrum E^{-1} both above and below the ankle. Refer to Figure 5.3 and Figure 5.4 for visual representations of the spectrum before and after correction. If the energy is below the ankle, only the subsequent correction is applied:

$$W_3' = 10^{(\mathrm{E}-\mathrm{E}_{\mathrm{min}})\cdot(\alpha-\Gamma)}. \tag{5.3}$$

If the energy is above the ankle, then the correction in Eq: 5.3 is applied, followed by an additional correction:

$$W_3 = W_3' \cdot 10^{(\mathrm{E}-\log(\mathrm{E_a}))\cdot(\Gamma_1-\Gamma_2)}. \tag{5.4}$$

Here, E represents the energy of the simulated particle, $E_{min} = 18.7$ in the units of $\log(\mathrm{E}_{min}/\mathrm{eV})$ is the chosen minimum energy, $\alpha = 1.0$ is the Spectral Index for the CRPropa 3, also in the units of $\log(\mathrm{E_a}/\mathrm{eV}) = 18.7$ which is the point at which the ankle is located. Then $\Gamma_1 = 3.29$ for the below ankle and $\Gamma_2 = 2.51$ for the above ankle.

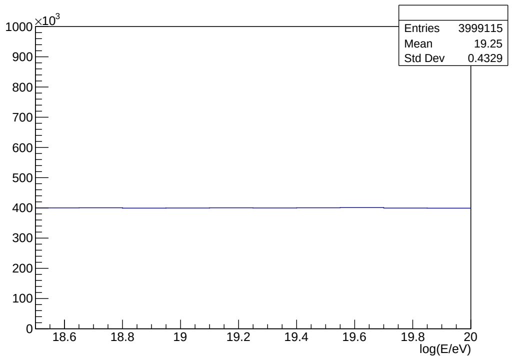

Figure 5.3: Before applying the correction for energy spectrum (W_3) to the simulated energy spectrum of CRPropa 3.

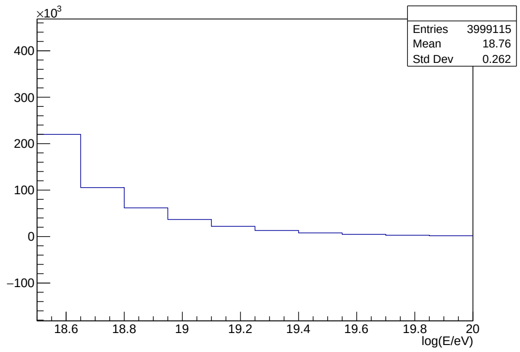

Figure 5.4: After the applying the correction for energy spectrum (W_3) to the simulated energy spectrum of CRPropa 3.

Resulting in:

$$W_{\mathrm{total}} = W_1 \times W_2 \times W_3, \tag{5.5}$$

where the weights are multiplied into a single value, which will be used as a correction factor for each individual simulated particle.

To summarize the CRPropa 3 simulated particle corrections. Once an isotropic simulated particle is selected, each of the above-mentioned weights is individually calculated for that particle and then collectively applied to it. This process is consistently executed for all particles generated by CRPropa 3, creating more realistic data that are not isotropic. The resulting distribution with respect to energy closely aligns with observed data.

5.4 Generating $X_{\mathbf{max}}$

The $X_{\max}$ values are generated for each simulated particle that successfully undergoes the correction procedures described in the preceding section of this chapter. The generation process leverages the generalized Gumbel distribution, which is a probability distribution often used in extreme value theory, producing a good fit for UHECR [54]. This is expressed as:

$$G(\mu, \sigma, \lambda) = \lambda^{\lambda} \cdot e^{-\lambda \frac{(x-\mu)}{\sigma} - \lambda e^{-\frac{(x-\mu)}{\sigma}}} . \tag{5.6}$$

The distribution is characterized by three parameters: μ, σ and λ, each of which is parametrized as a function of the primary particle's energy E and atomic number A. The parametrization takes the form:

$$\mu(A, E) = p_{0\mu} + p_{1\mu} \log_{10}\left(\frac{E}{E_0}\right) + p_{2\mu} \log_{10}^2\left(\frac{E}{E_0}\right) , \tag{5.7}$$

$$\sigma(A, E) = p_{0\sigma} + p_{1\sigma} \log_{10}\left(\frac{E}{E_0}\right) , \tag{5.8}$$

$$\lambda(A, E) = p_{0\lambda} + p_{1\lambda} \log_{10}\left(\frac{E}{E_0}\right) . \tag{5.9}$$

These polynomial expressions are constructed using predefined coefficient constants, which are determined through fits to data from the EPOS-LHC model [55]. Here E_0 represents a reference energy, typically chosen 10^{19} eV, to normalize the energy scale and facilitate the logarithmic transformations.

Once the parametrization is established, a dedicated loop iterates over the set of simulated particles, invoking a function that employs Eq: 5.6 to generate $X_{\max}$ for each particle.

Chapter 6

Mass-dependent anisotropy as a consequence of Galactic magnetic field using on-off Galactic plane selection

This study examines the effects of the GMF on the mass-dependent anisotropy in the arrival directions of particles above $10^{18.7}$ eV, as motivated by recent observations [8, 9] and detailed in Chapter 4. To investigate this effect's origin, the study propagates four types of particles in the GMF using the CRPropa 3 simulation (refer to Chapter 5.1). The simulated particles are then divide according to their arrival direction, determined by the on-off galactic plane, following [8]. Particles within $\pm\ 30°$ from the galactic plane in galactic latitude are classified as originating from the on-galactic plane, while the remaining particles are considered to be from the off-galactic plane. The analysis tests all possible mixtures of four primary particles (p, He, N, Fe). This is achieved by partitioning them into relative fractions, each varying by an increment of 10%, resulting in total of 286 possible combinations.

In the following Sections of this Chapter, this study investigates the case where the arrival directions of simulated particles are isotropic upon entering the Galaxy. The investigation reveals no significant mass-dependent anisotropies in the $\Delta\langle X_{\max}\rangle$, which is defined as the difference between the $\langle X_{\max}\rangle$ on-galactic and $\langle X_{\max}\rangle$ off-galactic plane. This is expected from the isotropic distribution, leaving the values displayed in the Figures 6.3, 6.4 and 6.5 as a statistical fluctuation. This is followed by an analysis of the anisotropic case, examining the effect of $\Delta\langle X_{\max}\rangle$ for the on-off galactic plane in relation to $\langle \ln(\mathrm{A})\rangle$ which represents the mean logarithmic mass A of a cosmic-ray mix, where A is the atomic mass number, and $\sigma^2(\ln(\mathrm{A}))$ which represents the spread of the mass distribution of primary cosmic rays. The last section of this chapter includes a specific case of a 50% - 50% proton-iron mixture, with a closer examination of the values of $\Delta\langle X_{\max}\rangle$ distribution for the on-off galactic plane.

All analyses in this chapter, covering multiple energy levels (18.5, 18.6, 18.7, 18.8

and 18.9) log(E/eV) revealed no significant differences in $\Delta\langle X_{\rm max}\rangle$ or $\Delta\sigma(X_{\rm max})$ when compared to the observed values. These observed values are $(9.1 \pm 1.6)\,{\rm g/cm^2}$ and $(5.9 \pm 2.1)\,{\rm g/cm^2}$ for $\Delta\langle X_{\rm max}\rangle$ and $\Delta\sigma(X_{\rm max})$ respectively at energy of 18.7 log(E/eV), as described in [8]. This remains valid in the updated version, where the $\Delta\langle X_{\rm max}\rangle$ value is approximately $5.0\,{\rm g/cm^2}$ [9].

6.1 Isotropic

The following figures, starting with Figure 6.1, represent the isotropic scenario of the arrival directions of cosmic rays at the edge of the Galaxy. In this scenario, the selection between the on-plane and off-plane regions of the Galaxy shows no significant values in $\Delta\langle X_{\rm max}\rangle$ or $\Delta\sigma(X_{\rm max})$.

Figure 6.2, represents the sky map visualized in galactic coordinates, confirms that the arrival directions remain isotropic. This reveals a uniform flux throughout, confirming Liouville's theorem ("an anisotropy cannot arise through deflections of an originally isotropic flux by a magnetic field" [4]). Figure 6.3 represents the relationship between $\Delta\langle X_{\rm max}\rangle$ and $\langle$ln(A)$\rangle$. This figure displays a range of values from the lowest (-0.3 ± 0.2) g/cm^2 to the highest (0.1 ± 0.2) g/cm^2, illustrating uniform changes in $\Delta\langle X_{\rm max}\rangle$ across the mixes without any significant deviations. This is expected from the isotropic distribution. Figure 6.4 represents the relationship between $\Delta\langle X_{\rm max}\rangle$ and $\sigma^2(ln(A))$ with values ranging from the lowest (-0.3 ± 0.2) g/cm^2 to the highest (0.1 ± 0.2) g/cm^2 with the overall behaviour showing a uniform distribution in all compositions with no significant value for any of the mixes. Once again this is to be expected from the isotropic distribution. Finally, Figure 6.5 explores the $\Delta\langle X_{\rm max}\rangle$ distribution for the on-off galactic plane in the extreme case represented by the mixture of a 50-50% of protons and iron nuclei, obtaining a $\Delta\langle X_{\rm max}\rangle$ value of (-0.1 ± 0.1) g/cm^2.

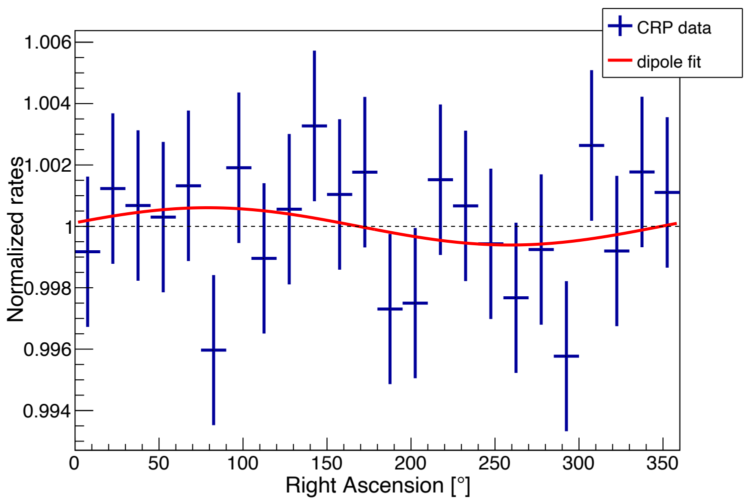

Figure 6.1: Isotropic distribution in Right Ascension (R.A) of the normalized rates of events with E $\geq 10^{18.7}$ eV. Red line represents the dipole fit of the simulated data to the first harmonic.

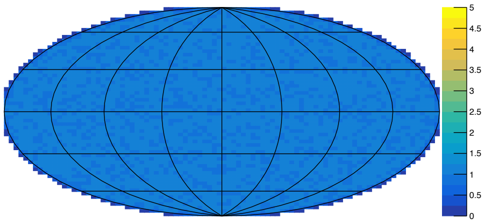

Figure 6.2: Mollweide projection with isotropic distribution of protons in galactic coordinates. Z-axis represent the flux intensity.

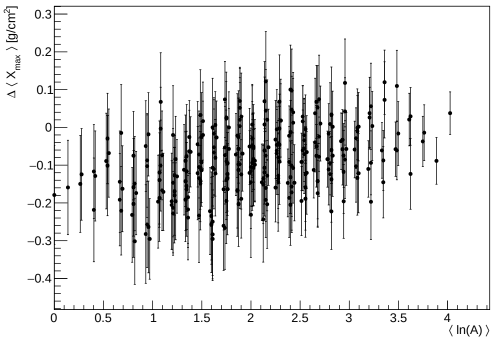

Figure 6.3: All 286 possible mixed compositions of p, He, N and Fe with isotropic distribution of arrival directions to the Galaxy are represented as a plot of $\Delta\langle X_{\max}\rangle$ versus $\langle\ln(\text{A})\rangle$ for energy above $10^{18.7}$ eV.

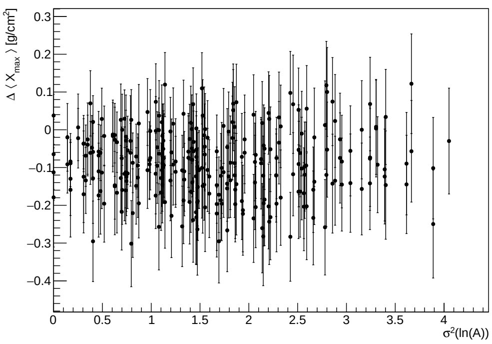

Figure 6.4: All 286 possible mixed compositions of p, He, N and Fe with isotropic distribution of arrival directions to the Galaxy are represented as a plot of $\Delta\langle X_{\max}\rangle$ versus $\sigma^2(\ln(\text{A}))$ for energy above $10^{18.7}$ eV.

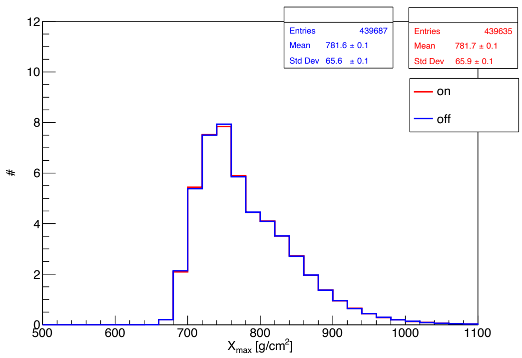

Figure 6.5: On-and off-galactic plane distributions of $X_{\max}$ for isotropic distribution of arrival directions to the Galaxy of 50/50 mix of protons and iron nuclei for energy above $10^{18.7}$ eV.

6.2 Anisotropic

The simulated particles, selected in accordance with [8, 9], possess energies exceeding $10^{18.7}$ eV and are reweighted (see Chapter 5.3) to more accurately reflect real-world observations from the Pierre Auger Observatory. The Auger dipole coordinates are specified as $(l, b) = (-127.0^\circ, -13.0^\circ)$ in galactic coordinates, with an amplitude of $0.065^{+0.012}_{-0.09}$ (see Figure 6.6). To attain amplitudes comparable to the observed Auger dipole, the simulated dipole amplitude is adjusted see Figure 6.7 to closely resemble the observed amplitude depicted in Figure 6.6. This results in a simulated amplitude of 0.08 at the edge of the Galaxy for all composition mixes.

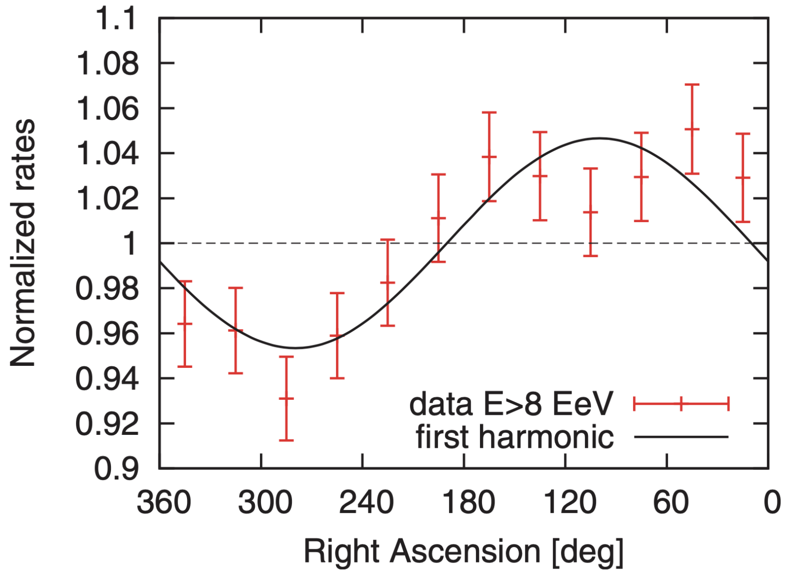

Figure 6.6: Normalized rate for 32,187 events with E $\geq$ 8 EeV, as a function of right ascension (integrated in declination). Error bars are 1σ uncertainties. The solid line shows the first-harmonic function, which displays good agreement with the data. The dashed line shows a constant function [4].

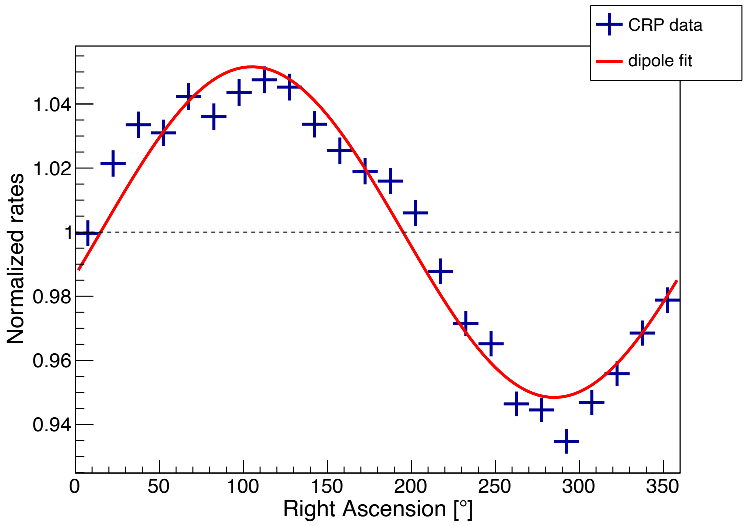

Figure 6.7: Fine tuned distribution in R.A of the normalized rates of events with E $\geq$ 8 EeV, to match [4]. Red line represents the dipole fit of the simulated data to the first harmonic function.

6.2.1 $\Delta\langle X_{\mathbf{max}}\rangle$ relation with Energy

To study potential energy dependencies, which include systematic uncertainties arising from energy calibration, several energy thresholds are chosen for the analysis in steps of 0.1 in log(E). No obvious energy dependencies of $\Delta\langle X_{\max}\rangle$ for the on-off galactic plane were found, as illustrated in Figure 6.8, which represents the extreme case of maximal mixing. This refers specifically to the mixing of 50% protons and 50% iron nuclei.

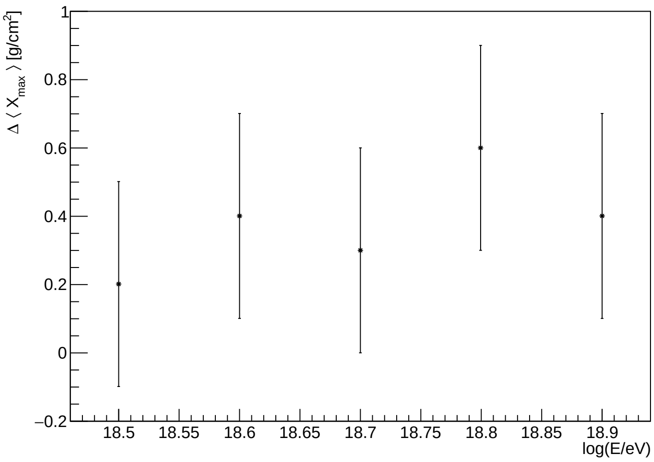

Figure 6.8: $\Delta\langle X_{\max}\rangle$ for on-off galactic plane and its corresponding energy thresholds for 50/50 mix of protons and iron nuclei.

6.2.2 $\Delta\langle X_{\max}\rangle$ vs $\langle \ln(A)\rangle$

To further investigate mass-dependent anisotropy, an energy threshold of $10^{18.7}$ eV is chosen, in accordance with [8, 9], due to the highest observed differences at this energy level. Subsequently, we obtained values of $\Delta\langle X_{\max}\rangle$ for the on-off Galactic plane, which range from a minimum of (-0.2 ± 0.2) g/cm^2 to a maximum of (0.8 ± 0.2) g/cm^2 see Figure 6.9.

From the aforementioned figure, it is evident that the overall behavior exhibits a non-significant $\Delta\langle X_{\max}\rangle$ compared to the isotropic behavior displayed in Figure 6.3. This implies that there is either no correlation or an insignificant correlation between the size of the cosmic ray composition mixing and $\Delta\langle X_{\max}\rangle$.

Additionally, no $\Delta\langle X_{\max}\rangle$ value approaches the observed magnitude. This finding is in direct contradiction with the results presented in [8] and also its updated version [9], which shows smaller differences compared to the initial paper, hence the findings are in disagreement with the initial hypothesis from the aforementioned papers.

6.2.3 $\Delta\sigma(X_{\max})$ vs $\langle \ln(A)\rangle$

A similar analysis can be made regarding Figure 6.10. This figure illustrates $\Delta\sigma(X_{\max})$, representing the difference in the spread of $X_{\max}$, and the variance between the on-plane and off-plane regions of the Galaxy. As we approach the maximally mixed beam around the middle of the X-axis, the difference in the width of the $(X_{\max})$

distribution appears to progressively increase. However, the difference between the on-plane and off-plane regions of the Galaxy shows a maximum of (0.8 ± 0.2) g/cm^2. Considering the errors, this more closely resembles an isotropic scenario rather than the observations noted in [8, 9].

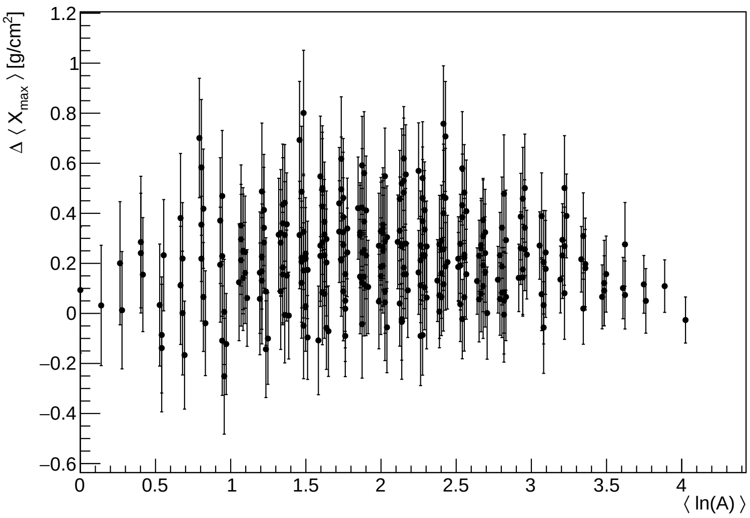

Figure 6.9: All 286 possible mixed compositions of p, He, N and Fe with anisotropic distribution of arrival directions to the Galaxy are represented as a plot of $\Delta\langle X_{\max}\rangle$ versus $\langle \ln(\mathrm{A})\rangle$ for energy above $10^{18.7}$ eV. According to on-off Galactic plane split.

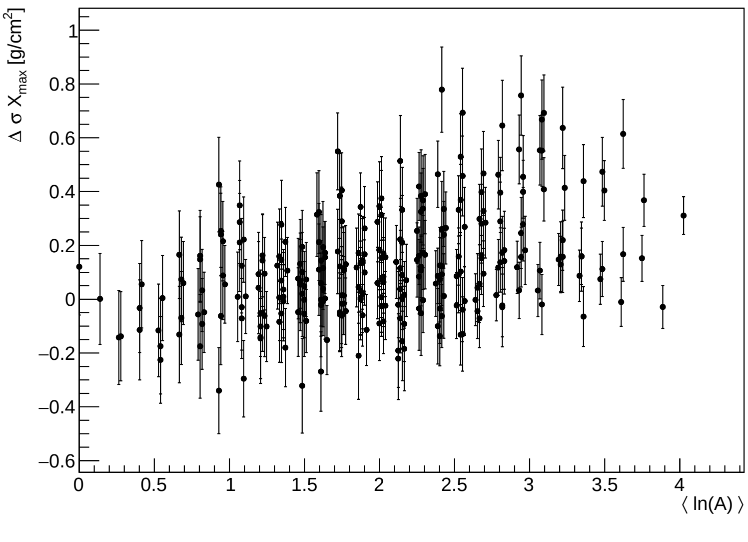

Figure 6.10: All 286 possible mixed compositions of p, He, N and Fe with anisotropic distribution of arrival directions to the Galaxy are represented as a plot of $\Delta\sigma(X_{\max})$ versus $\langle \ln(\mathrm{A})\rangle$. For energy above $10^{18.7}$ eV. According to on-off Galactic plane split.

6.2.4 $\Delta\langle X_{\mathbf{max}}\rangle$ vs $\sigma^2(\mathbf{ln(A)})$

Similar to the previous Section, the $\Delta\langle X_{\max}\rangle$ for the on-off Galactic plane ranges from a minimum of (-0.2 ± 0.3) g/cm^2 to a maximum of (0.8 ± 0.3) g/cm^2 for energies above $10^{18.7}$ eV; see Figure 6.11. The overall behavior demonstrates a non-significant $\Delta\langle X_{\max}\rangle$ value. Furthermore, considering the errors associated with these values, it appears that the behavior more closely resembles a statistical fluctuation similar to that observed in the isotropic scenario depicted in Figure 6.4. This suggests that there is either no correlation or only an insignificant correlation between the extent of cosmic ray composition mixing and the $\Delta\langle X_{\max}\rangle$ value. Additionally, none of the values observed are of similar magnitude to those reported in [8] or its update [9].

6.2.5 $\Delta\sigma(X_{\mathbf{max}})$ vs $\sigma^2(\mathbf{ln(A)})$

Once again, we see the maximum value of $\Delta\sigma(X_{\max})$ is (0.8 ± 0.3) g/cm^2, located in the region corresponding to an approximately fully mixed beam, around the middle value between 0 and 4 on the x-axis. The following section of this chapter will examine the fully mixed beam in greater detail.

In conclusion, Figure 6.12 appears to depict isotropic fluctuations, without any significant values observed.

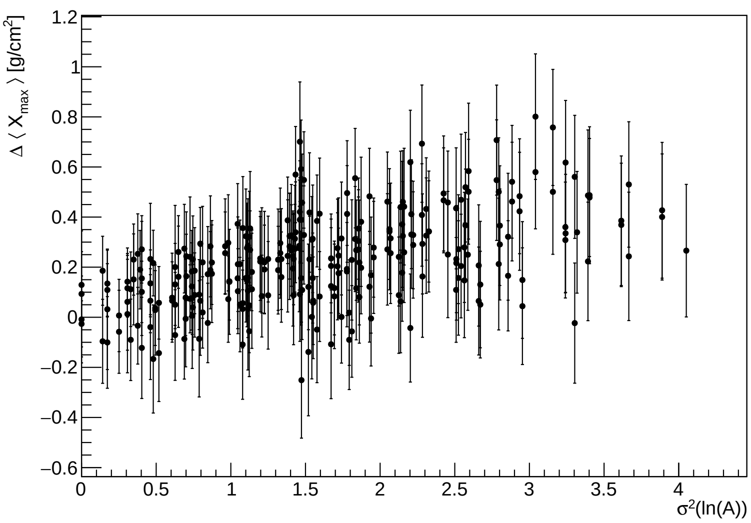

Figure 6.11: All 286 possible mixed compositions of p, He, N and Fe with anisotropic distribution of arrival directions to the Galaxy are represented as a plot of $\Delta\langle X_{\max}\rangle$ versus σ^2(ln(A)) For energy above $10^{18.7}$ eV. According to on-off Galactic plane split.

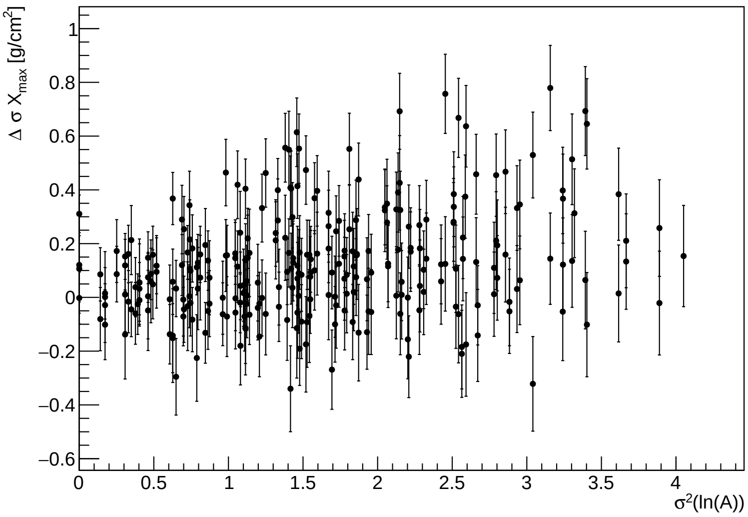

Figure 6.12: All 286 possible mixed compositions of p, He, N and Fe with anisotropic distribution of arrival directions to the Galaxy are represented as a plot of $\Delta\sigma(X_{\max})$ versus $\sigma^2(\ln(\mathrm{A}))$ For energy above $10^{18.7}$ eV. According to on-off Galactic plane split.

6.2.6 50% - 50% proton - iron mix

The highest values of $\Delta\langle X_{\max}\rangle$ and $\Delta\sigma(X_{\max})$ for the on-off Galactic plane are anticipated in the extreme case depicted in Figure 6.13, which consists of a 50-50% mixture of protons and iron nuclei.

A detailed examination of the non-significant values $\Delta\langle X_{\max}\rangle$ and $\Delta X_{\max}$ is presented in Table: 6.1. The conclusion is the same as the previous Sections of this Chapter, the aforementioned figure reveals a closer resemblance to the isotropic scenario showed in Figure 6.5. Once again, its value does not closely resemble the findings mentioned in [8] nor its updated version [9].

On-Off Galactic plane		
50%-50% proton-iron	ΔX_{max} [g/cm^2]	$\Delta\sigma(X_{max})$[g/cm^2]
Isotropic	0.1 ± 0.1	0.2 ± 0.1
Auger Dipole	0.3 ± 0.3	0.2 ± 0.2

Table 6.1: Table containing the On-Off galactic plane $\Delta\langle X_{\max}\rangle$ and $\Delta\sigma(X_{\max})$ values with E $\geq 10^{18.7}$ eV, for extreme case of proton-iron mix. The corresponding errors are calculated using the error values taken from Figure 6.13 which are then summed under quadrature.

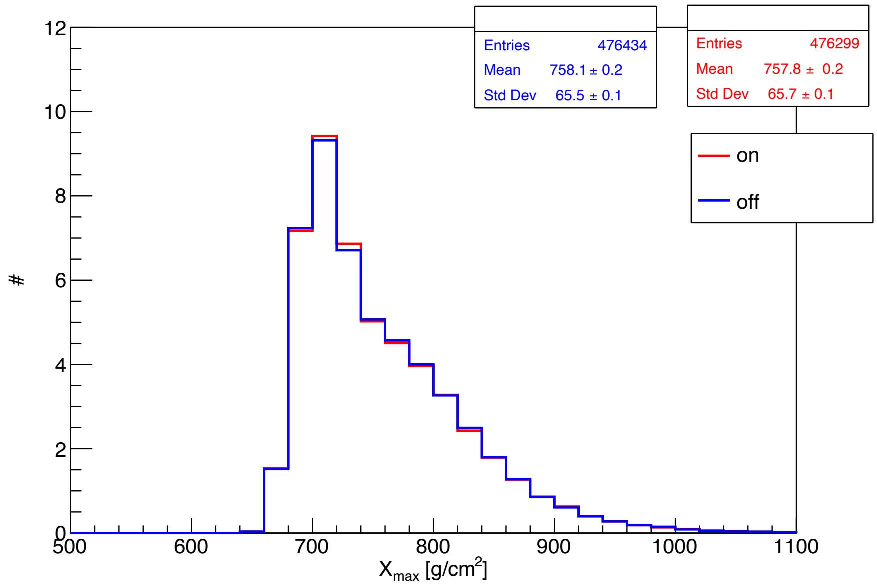

Figure 6.13: On-and off-galactic plane distributions of $X_{\max}$ for anisotropic distribution of arrival directions to the Galaxy of 50/50 mix of protons and iron nuclei for energy above $10^{18.7}$ eV.

6.3 Chapter summary

To conclude this Chapter, the performance of the analysis method proposed in [8, 9] yields an insignificant result, with maximum magnitudes of (0.8 ± 0.2) g/cm^2 and (0.8 ± 0.3) g/cm^2 for $\Delta\langle X_{\max}\rangle$ and $\Delta\sigma(X_{\max})$ respectively. These findings are not in alignment with the observed values of (9.1 ± 1.6) g/cm^2 and (5.9 ± 2.9) g/cm^2 for $\Delta\langle X_{\max}\rangle$ and $\Delta\sigma(X_{\max})$ respectively, at energies greater than $10^{18.7}$ eV as reported in [8], nor do they align with the updated values stated in [9].

Chapter 7

Mass-dependent anisotropy as a consequence of Galactic magnetic field using on-off dipole selection

The initial analysis presented in Chapter 6, shows that no significant values of $\Delta\langle X_{\max}\rangle$ or $\Delta\sigma(X_{\max})$ are obtained, which leads to further investigation conducted in the following Sections of this Chapter. Here, the impact of the GMF on the mass-dependent anisotropy in the arrival directions of particles with energies above $10^{18.7}$ eV, as observed in [8, 9] is explored. As in the previous Chapter, four types of particles; proton, helium, nitrogen and iron are propagated within the GMF using the CRPropa 3 simulations. However, this time, the simulated particles are categorised according to their on-off dipole arrival direction, following the measurements outlined by [4]. The dipole of interest is the Auger-like dipole described in Chapter 6.2. Particles arriving from 0 to 196° in the right ascension (R.A) are classified as on-dipole, while all other particle directions are off-dipole. The cut value of 196° is established using Figure 6.7 at a point where the dipole fit intersects the unit line. It is important to mention that the aforementioned figure described in Chapter 6.2 is the simulated dipole tailored to resemble the observed Auger dipole. The analysis is then carried out for different mixtures of the four primary particles that are once again constructed by partitioning them into relative fractions, each varying by increments of 10%, resulting in a total of 286 possible combinations.

In the following Sections of this Chapter, the anisotropic distribution of simulated particles entering the Galaxy is investigated, and subsequently the effects of $\Delta\langle X_{\max}\rangle$ and $\Delta\sigma(X_{\max})$ in the on-off dipole comparison. Both $\Delta\langle X_{\max}\rangle$ and $\Delta\sigma(X_{\max})$ are compared in relation to $\langle\ln(A)\rangle$ and $\sigma^2(\ln(A))$. This is followed by a Section that includes a specific case of the $\Delta\langle X_{\max}\rangle$ and $\Delta\sigma(X_{\max})$ distributions of the on-off dipole with a mixture of 50% proton and 50% iron.

All analyses carried out in this Chapter yield significant values in $\Delta\langle X_{\max}\rangle$, though not as much in $\Delta\sigma(X_{\max})$. Unfortunately, their magnitudes do not reach the observed values of (9.1 ± 1.6) g/cm^2 and (5.9 ± 2.1) g/cm^2 for $\Delta\langle X_{\max}\rangle$ and $\Delta\sigma(X_{\max})$, respectively, as described in [8]. This remains true even when considering its updated version, where the value of $\Delta\langle X_{\max}\rangle$ is approximately $5.0\,\mathrm{g/cm^2}$ [9]. However, the analysis presented here demonstrates some mass-dependent anisotropy caused by the mixing of the particles with respect to the dipole split.

7.0.1 $\Delta\langle X_{\mathbf{max}}\rangle$ relation with Energy

To investigate the potential energy dependencies, which also include systematic uncertainties stemming from energy calibration, several energy thresholds are chosen for the analysis, incrementing in steps of 0.1 log(E). No obvious energy dependence of $\Delta\langle X_{\max}\rangle$ is found, as illustrated in Figure 7.1. This figure represents the scenario of maximal mixing, specifically the 50%-50% proton-iron for the on-off dipole split test.

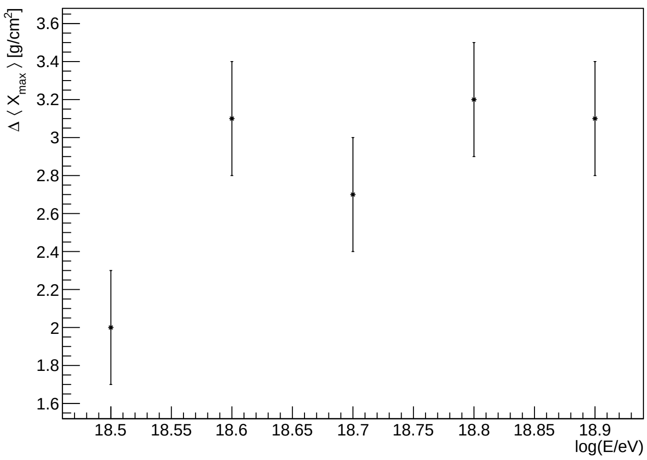

Figure 7.1: $\Delta\langle X_{\max}\rangle$ for on-off dipole and its corresponding energy thresholds for 50/50 mix of protons and iron nuclei.

7.0.2 $\Delta\langle X_{\mathbf{max}}\rangle$ vs $\langle\ln(\mathrm{A})\rangle$

This Section is focusing on particle energies above $10^{18.7}$ eV as reported in [8, 9]. Resulting in a significant $\Delta\langle X_{\max}\rangle$ for the on-off dipole split, with a maximal value of (3.3 ± 0.5) g/cm^2 (refer to Figure 7.2). The overall behavior exhibits a graph with an 'umbrella shape', as described in [10]. This pattern implies a potential relationship between $\Delta\langle X_{\max}\rangle$ and $\sigma^2(\ln(\mathrm{A}))$, suggesting that mass-dependent anisotropy is associated with the size of cosmic ray composition mixing.

7.0.3 $\Delta\sigma(X_{\mathbf{max}})$ vs $\langle\ln(\mathrm{A})\rangle$

The variance of $X_{\max}$ shown in Figure 7.3 displays the values of $\Delta\sigma(X_{\max})$ with respect to the mean logarithmic mass of the cosmic-ray mix, for the on-off dipole split. The maximal value observed, when approaching a maximally mixed beam around the middle of the X-axis, is (0.6 ± 0.2) g/cm^2. While the overall trend is consistent with the proposed hypothesis, the values do not align with the observed values of (5.9 ± 0.2) g/cm^2 as reported in [8, 9]. It is noteworthy to mention that these discrepancies do not categorize the phenomenon as isotropic (see Chapter 6.1).

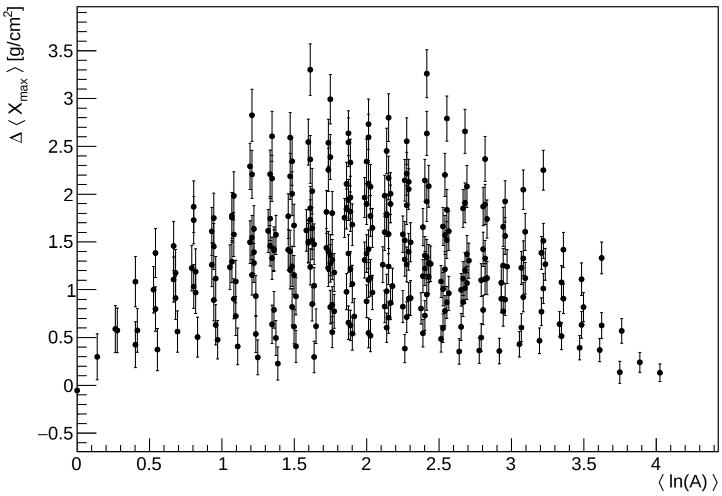

Figure 7.2: All 286 possible mixed compositions of p, He, N and Fe with anisotropic distribution of arrival directions to the Galaxy are represented as a plot of $\Delta\langle X_{\max}\rangle$ versus $\langle \ln(A)\rangle$. For energy above $10^{18.7}$ eV. According to on-off dipole split.

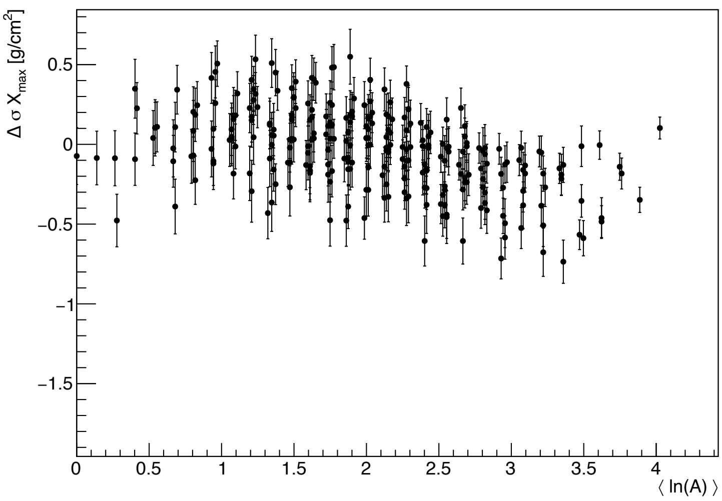

Figure 7.3: All 286 possible mixed compositions of p, He, N and Fe with anisotropic distribution of arrival directions to the Galaxy are represented as a plot of $\Delta\sigma X_{\max}$ versus $\langle \ln(A)\rangle$. For energy above $10^{18.7}$ eV. According to on-off dipole split.

7.0.4 $\Delta\langle X_{\mathbf{max}}\rangle$ vs $\sigma^2(\mathbf{ln(A)})$

Similarly to the Section 7.0.2, the $\Delta\langle X_{\max}\rangle$ for the on-off dipole ranges from a minimum of (-0.1 $\pm$ 0.2) g/cm^2 to a maximum of (3.3 $\pm$ 0.5) g/cm^2 for energies above $10^{18.7}$ eV, as illustrated in Figure 7.4. The overall behavior is characterized by points tightly concentrated forming a line like shape, indicating an increasing trend of $\Delta\langle X_{\max}\rangle$ with respect to σ^2(ln(A)). This suggests minimal variation in $\Delta\langle X_{\max}\rangle$ across different mix compositions, implying that the $\Delta\langle X_{\max}\rangle$ values remain relatively stable for each composition mix originating from a single extragalactic dipole. Consequently, similar to the findings in Section 7.0.2, this pattern indicates a correlation between $\Delta\langle X_{\max}\rangle$ and the size of cosmic ray composition mixing.

7.0.5 $\Delta\sigma(X_{\mathbf{max}})$ vs $\sigma^2(\mathbf{ln(A)})$

In Figure 7.5, the $\Delta\sigma^2(X_{\max})$ reach a maximum of (0.6$\pm$0.2) g/cm^2, aligning with the values reported in Section 7.0.3. These values form a nearly straight and compact line of points, exhibiting fluctuations within $\pm$0.5 g/cm^2. This indicates a non-significant effect on the width of $\Delta\sigma(X_{\max})$ across different degree of mixing. It is important to note that, while these values are higher than those observed for isotropic behaviors (as discussed in Chapter 6.1) they do not closely match the observations reported in [8, 9].

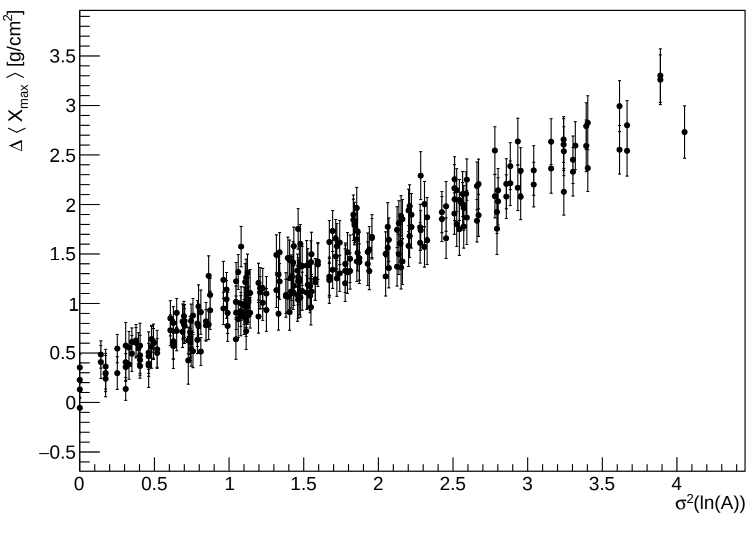

Figure 7.4: All 286 possible mixed compositions of p, He, N and Fe with anisotropic distribution of arrival directions to the Galaxy are represented as a plot of $\Delta\langle X_{\max}\rangle$ versus σ^2(ln(A)). For energy above $10^{18.7}$ eV. According to on-off dipole split.

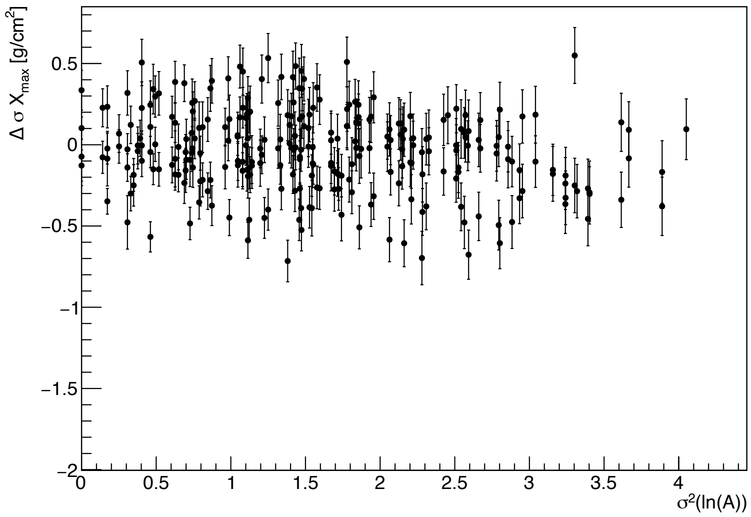

Figure 7.5: All 286 possible mixed compositions of p, He, N and Fe with anisotropic distribution of arrival directions to the Galaxy are represented as a plot of $\Delta\sigma(X_{\max})$ versus $\sigma^2(\ln(\mathrm{A}))$. For energy above $10^{18.7}$ eV. According to on-off dipole split.

7.0.6 50% - 50% proton - iron mix

The highest values of $\Delta\langle X_{\max}\rangle$ and $\Delta\sigma(X_{\max})$ for the on-off dipole are anticipated in the extreme case, as depicted in Figure 7.6. This case involves a mixture consisting of 50 % protons and 50% iron nuclei.

A thorough examination reveals significant $\Delta\langle X_{\max}\rangle$ values and less significant $\Delta\sigma(X_{\max})$ values, as detailed in Table: 7.1. These findings indicate a mass-dependent anisotropic behavior related to the size of the cosmic ray mix. In addition, these values do not closely resemble the magnitudes mentioned in [8] or its updated version [9]. Also from the previous Sections of this Chapter, it is clearly visible that the maximal case in both the $\langle X_{\max}\rangle$ and $\sigma(X_{\max})$ is found in different mix composition then the proton - iron mix.

On-Off Auger Dipole cut		
50%-50% proton-iron	ΔX_{max} [g/cm^2]	$\Delta\sigma(X_{max})$[g/cm^2]
Isotropic	0.1 ± 0.1	0.2 ± 0.1
Auger Dipole	2.7 ± 0.3	0.06 ± 0.1

Table 7.1: Table containing the On-Off dipole $\Delta\langle X_{\max}\rangle$ and $\Delta\sigma(X_{\max})$ values with $\mathrm{E} \geq 10^{18.7}$ eV, for extreme case of proton-iron mix. The corresponding errors are calculated using the error values taken from Figure 7.6 which are then summed under quadrature.

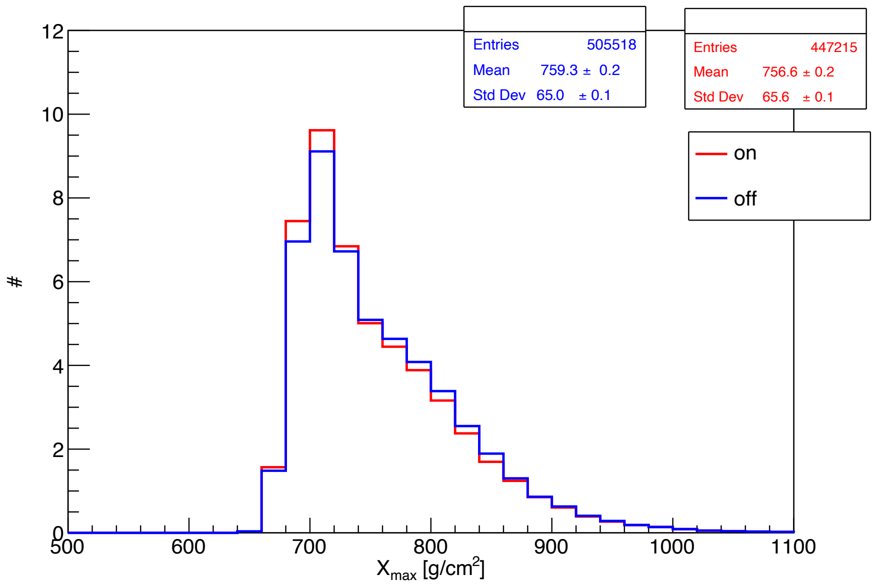

Figure 7.6: On-off dipole plane distributions of $X_{\max}$ for anisotropic distribution of arrival directions to the Galaxy of 50/50 mix of protons and iron nuclei for energy above $10^{18.7}$ eV.

7.1 Chapter summary

To summarize this Chapter, the performance of the analytical method, based on the measurements from [4] of the Auger-like dipole yields significant maximum magnitudes of (3.3 ± 0.3) g/cm^2 and (0.06 ± 0.1) g/cm^2 for $\Delta\langle X_{\max}\rangle$ and $\Delta\sigma(X_{\max})$ respectively. These values do not reach the magnitudes of $\Delta\langle X_{\max}\rangle = 9.1 \pm 1.6$ [g/cm^2] and $\Delta\sigma(X_{\max}) = 5.9 \pm 2.9$ [g/cm^2] as was observed in [8] or its updated version [9]. However, the analysis does demonstrate that mass-dependent anisotropy is influenced by the size of cosmic ray composition mixing, particularly when considering a single Auger-like dipole.

Chapter 8

Mass-dependent anisotropy as a consequence of Galactic magnetic field influenced by properties of an extragalactic dipole

Upon the successful reproduction of a significant value for $\Delta\langle X_{\max}\rangle$ in Chapter 7, this chapter will adopt a similar methodology and settings. With a primary distinction in the differing positions and amplitudes of the extragalactic dipole for each particle composition. This approach facilitates an in-depth analysis of the GMF influence on the mass-dependent anisotropy in particle arrival direction, particularly to the change in extragalactic dipole. The analysis utilizes a dataset of 1005 individual extragalactic dipoles with varying (l, b) coordinates and amplitudes, as provided by [46]. These dipole values fall within 2σ of the observed Auger dipole, and do not encompass the entire ln(A) mass distribution. This is the consequence of the paper [46] which also simulates particles using CRPropa 3 with JF12 as its GMF model and delves into the examination of the specific amplitude and dipole direction that could exhibit suppression for particular compositions. This reveals that some solutions, particularly for heavier compositions mixes, do not align within the 2σ of the observed Auger dipole. For a more comprehensive analysis of the methodology used, see the above-mentioned paper.

Additional analysis of individual extragalactic dipole solutions was carried out to check if there exist directional biases in the selection of the 1005 extragalactic dipoles. Figure 8.1 confirms the absence of such biases by comparing these dipoles to the complete set of solutions depicted in the original Figure 8.2 from [46]. Additionally, the selected dipoles sufficiently cover the required spread for the analyses proposed in this Chapter.

Subsequent sections of this chapter will investigate the anisotropic distribution of simulated particles entering the Galaxy. This include an analysing of $\Delta\langle X_{\max}\rangle$ and $\Delta\sigma(X_{\max})$ for the on-off dipole in relation to $\langle\ln(\mathrm{A})\rangle$ and $\sigma^2(\ln(\mathrm{A}))$ considering both composition mixing and extragalactic dipole positions. Then additional section will focus on a specific case study involving a 50% - 50% proton - iron mix for the $\Delta\langle X_{\max}\rangle$ distribution of the on-off dipole. All analyses in this chapter yield significant values in $\Delta\langle X_{\max}\rangle$ and $\Delta\sigma(X_{\max})$, although their magnitudes did not exceed the maximal values obtained in in Chapter 7, however the spread of $\sigma^2(ln(A))$ is more dispersed in comparison to Chapter 7.0.4 suggesting that the position of an extragalactic dipole has an effect on the $\Delta\langle X_{\max}\rangle$ values, as further explored in Figure 8.8 which then have closer look at the specific dipoles and their corresponding values showing mass-dependent anisotropy.

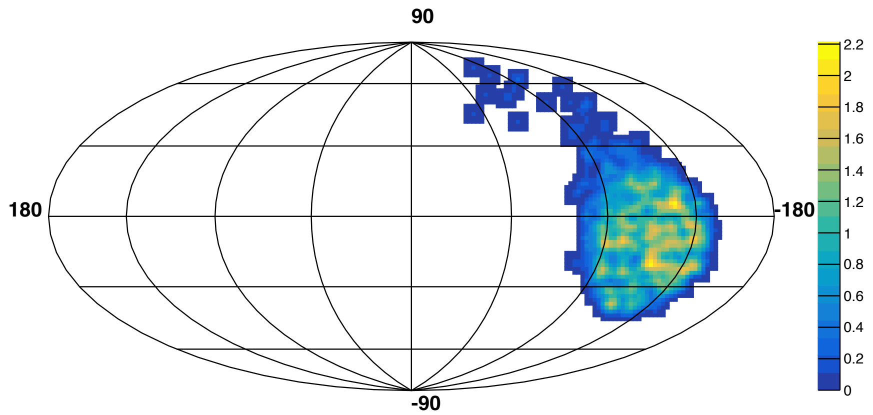

Figure 8.1: The directions of the 1005 possible extragalactic dipole provided by [46], whose value are within 2σ of the observed Auger dipole with the JF12 GMF model plotted in Galactic coordinates with Gaussian smoothing. Z-axis represent the relative concentration of chosen dipoles position.

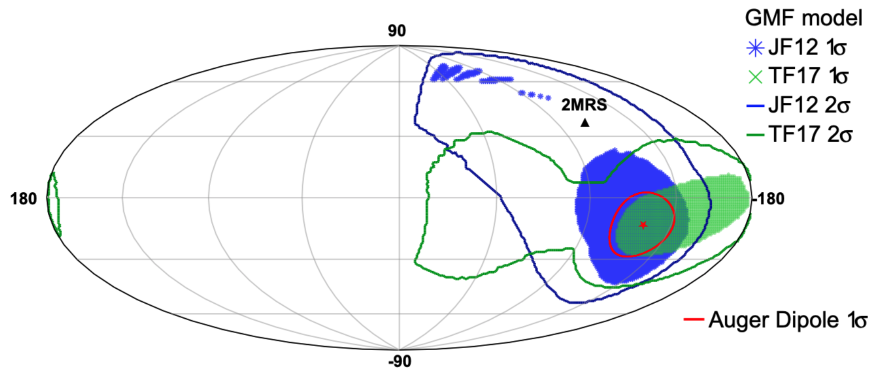

Figure 8.2: The directions of the extragalactic dipole in Galactic coordinates found for all different mass composition scenarios for the JF12 and TF17 models of GMF within 1σ. Areas of possible directions of the extragalactic dipole compatible with the measurements within 2σ are shown by blue and green lines for JF12 and TF17 models, respectively. The 1σ contour of the dipole measured by the Pierre Auger Observatory above 8 EeV is shown in red and direction of the 2MRS dipole is displayed with a black triangle marker [46].

8.0.1 $\Delta\langle X_{\mathbf{max}}\rangle$ vs $\langle\ln(\mathrm{A})\rangle$

The significant $\Delta\langle X_{\max}\rangle$ for particles with energies above $10^{18.7}$ eV, with a corresponding maximal value of (3.0 ± 0.1) g/cm^2 see Figure 8.3. The overall behaviour displays a familiar "umbrella shape" graph from [10] with its high mass compositions missing and also the position of the highest $\Delta\langle X_{\max}\rangle$ being shifted when compared to Chapter 7.0.2. This implies that there might exist extragalactic dipole positions which can cause such a effect in the $\Delta\langle X_{\max}\rangle$ with respect to $\langle\ln(\mathrm{A})\rangle$, in addition to the size of cosmic ray composition mixing.

8.0.2 $\Delta\sigma(X_{\mathbf{max}})$ vs $\langle\ln(\mathrm{A})\rangle$

Focusing on the relation between the $\Delta X_{\max}$ width and the mean logarithmic mass of the mixed beam for particles with energies exceeding $10^{18.7}$ eV. A significant values and also the the overall behaviour of the trend is obtained which shows that a changes in the dipole positions or/and amplitudes will subsequently result in different variances of $\Delta\sigma(X_{\max})$, as visible per Figure 8.4. One should expect what is weakly observed in Figure 7.3 from previous Chapter, however the increase in the mean logarithmic mass of the mixed beam correlates with a subsequent rise in the $\Delta\sigma(X_{\max})$. This is a indication that heavier elemental compositions, or its mixtures, are positioned further from the dipole compared to their lighter counterparts. With its maximal value to be (2.5 ± 0.1) g/cm^2. This is much higher then what was obtained in Chapter 7.0.3.

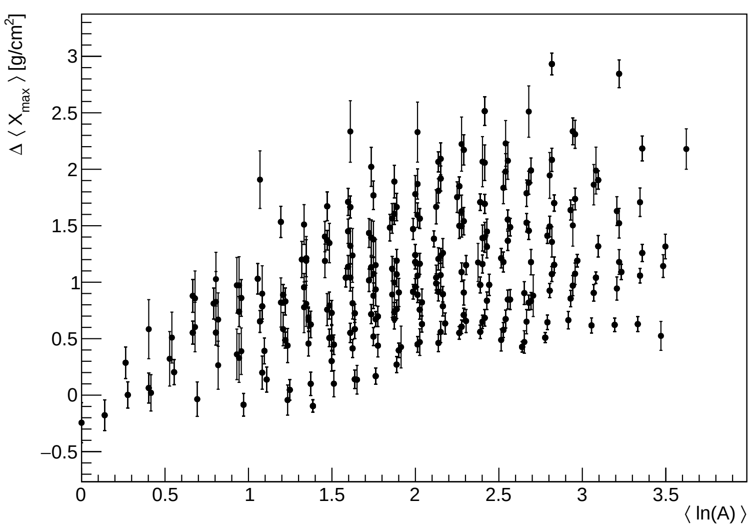

Figure 8.3: For energy above $10^{18.7}$ eV, all 1005 extragalatic dipole directions with corresponding mixed compositions of p, He, N and Fe with anisotropic distribution of arrival directions to the Galaxy are represented as a plot of $\Delta\langle X_{\max}\rangle$ versus $\langle\ln(\mathrm{A})\rangle$, using the on-off dipole split.

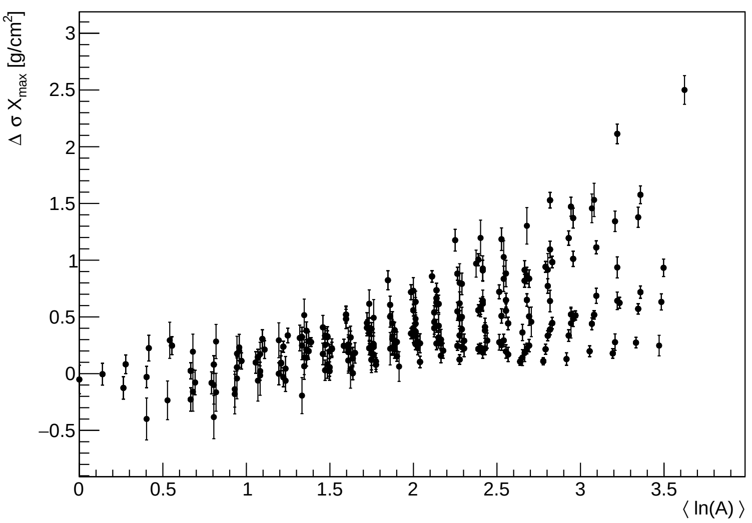

Figure 8.4: For energy above $10^{18.7}$ eV, all 1005 extragalatic dipole directions with corresponding mixed compositions of p, He, N and Fe with anisotropic distribution of arrival directions to the Galaxy are represented as a plot of $\Delta\sigma(X_{\rm max})$ versus $\langle \ln(\mathrm{A}) \rangle$, using the on-off dipole split.

8.0.3 $\Delta\langle X_{\rm max}\rangle$ vs $\sigma^2(\ln(\mathrm{A}))$

In the analysis of the degree of mixing, findings align with those illustrated in Figure 8.3. The Figure 8.5 shows the value of $\Delta\langle X_{\rm max}\rangle$ for on-off dipole to range from the lowest of (-0.2 ± 0.2) g/cm^2 up to the largest values of (3.0 ± 0.1) g/cm^2. The overall behavior reinforces the correlation between the size of cosmic ray composition mixing and the $\Delta\langle X_{\rm max}\rangle$ value, as previously indicated in Figure 8.3 and now additionally in Figure 8.5. This evidence strengthens the hypothesis that different extragalactic dipoles can yield varying $\Delta\langle X_{\rm max}\rangle$ values. Notably, some dipoles exhibit almost double the spread in $\Delta\langle X_{\rm max}\rangle$ compared to Figure 7.4, suggesting that certain extragalactic dipoles may have a more pronounced effect on the $\Delta\langle X_{\rm max}\rangle$ then other.

8.0.4 $\Delta\sigma(X_{\rm max})$ vs $\sigma^2(\ln(\mathrm{A}))$

Examining the different values of the beam mixing represented by $\sigma^2(\ln(\mathrm{A}))$ Figure 8.6, one can immediately see that the values differ from Figure 7.5 from previous Chapter. Specifically Figure 8.6 reveals a maximal $\Delta\sigma(X_{\rm max})$ value of (2.5 ± 0.1) g/cm^2. While this value on its own does not tell much however when compared to the aforementioned Figure from previous Chapter, then we can see that the introduction of different extragalatic dipoles leads to varied values for the same mixtures. This is another indication that different dipoles contribute to increased differences in $\Delta X_{\rm max}$.

Another observation is that for non mixed or minimally mixed beam up to the value 1.5 of $\sigma^2(\ln(\mathrm{A}))$ the points remain more compact and form a straight, compact line within a ± 0.5 g/cm^2 range, similar to the pattern observed in Figure 7.5. Then beyond the position where the peak value is located (approx 1.5 of $\sigma^2(\ln(\mathrm{A}))$), the points become more dispersed and less compact. In cases of more intensive mixing, the value sometimes doubles. This is a indication that combination of different dipoles together with mixing brings higher impact on the differences in $\Delta\sigma(X_{\max})$.

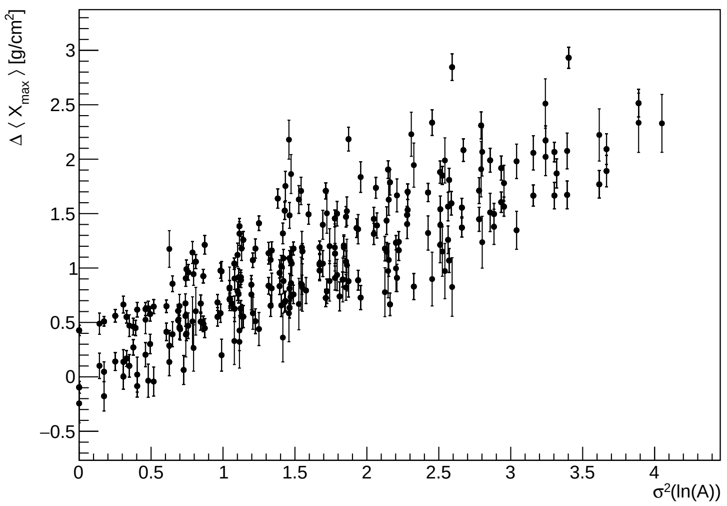

Figure 8.5: For energy above $10^{18.7}$ eV all 1005 extragalatic dipole directions with corresponding mixed compositions of p, He, N and Fe with anisotropic distribution of arrival directions to the Galaxy are represented as a plot of $\Delta\langle X_{\max}\rangle$ versus $\sigma^2(\ln(\mathrm{A}))$, using the on-off dipole split.

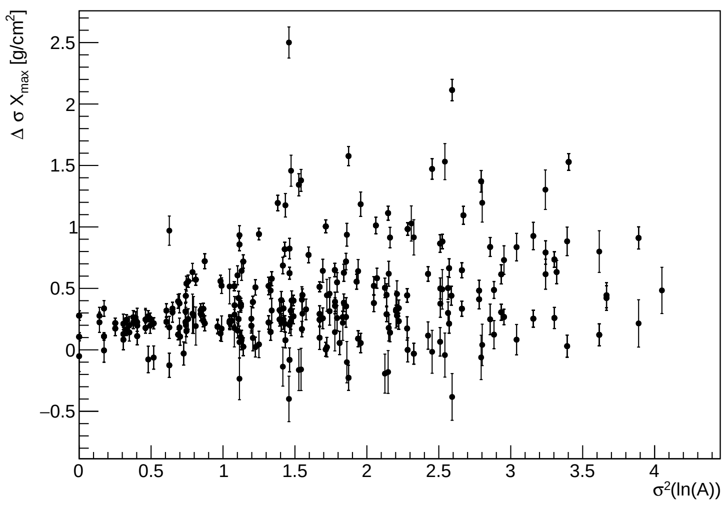

Figure 8.6: For energy above $10^{18.7}$ eV all 286 possible mixed compositions of p, He, N and Fe with anisotropic distribution of arrival directions to the Galaxy are represented as a plot of $\Delta\sigma(X_{\max})$ versus $\sigma^2(\ln(\mathrm{A}))$, using the on-off dipole split.

8.0.5 50% - 50% proton - iron mix

Once again the highest $\Delta\langle X_{\max}\rangle$ and $\Delta\sigma(X_{\max})$ for the on-off dipole are anticipated in the extreme case depicted in Figure 8.7, which consists of a mixture of a 50-50% of protons and iron nuclei. A comprehensive analysis reveals significant $\Delta\langle X_{\max}\rangle$ and $\Delta\sigma(X_{\max})$ values, which, however, do not exceed the magnitudes obtained for a single dipole in Chapter 7.0.6. Furthermore, these values are not the highest anticipated, as evidenced by Figure 8.3 and Figure 8.5 which demonstrate that higher values are present in beams with different compositions than the one analyzed here, similarly as in Chapter 7.0.6.

Obtained values are presented in the Table: 8.1, indicating a mass-dependent anisotropy behaviour toward size of cosmic ray mix.

On-Off Dipole cut		
50%-50% proton-iron	ΔX_{max} [g/cm^2]	$\Delta\sigma(X_{max})$[g/cm^2]
Isotropic	0.1 ± 0.1	0.23 ± 0.1
Extragalactic dipole	2.3 ± 0.2	0.11 ± 0.1

Table 8.1: Table containing the On-Off dipole $\Delta\langle X_{\max}\rangle$ and $\Delta\sigma(X_{\max})$ values with $E \geq 10^{18.7}$ eV, for extreme case of proton-iron mix. The corresponding errors are calculated using the error values taken from Figure 8.7 which are then summed under quadrature.

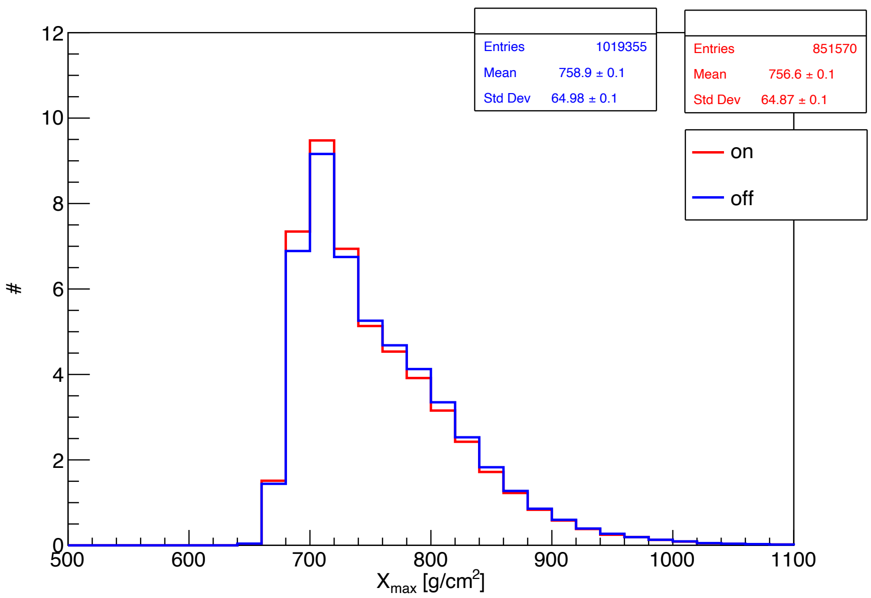

Figure 8.7: On-off dipole distributions of $X_{\max}$ for anisotropic distribution of arrival directions to the Galaxy of 50/50 mix of protons and iron nuclei for energy above $10^{18.7}$ eV.

8.1 Chapter summary

To summarize this Chapter, the analytical approach introduced in Chapter 7 has been applied to various extragalactic dipole scenarios, as detailed in [46]. The findings indicate that while the $\Delta\langle X_{\max}\rangle$ values obtained did not exceed the maxima observed in Chapter 7 for the chosen Auger-like dipole scenario, but the $\Delta(\sigma X_{\max})$ values did surpass those in the same Chapter. However neither set of values reached the magnitudes reported in [8, 9].

Further analysis, highlighted in Figure 8.4 show that beside the mixing also the different dipoles values causing the spread of the $\Delta X_{\max}$, this is closely explained in the Section 8.0.2 of this Chapter. Additionally, Figure 8.5 and Figure 8.6 demonstrate a greater spread in values compared to a single Auger-like dipole scenario discussed in Chapter 7.0.4. Suggests that the position of an extragalactic dipole has an effect on the $\Delta\langle X_{\max}\rangle$ values, this is then examined in Figure 8.8 which shows the $\Delta\langle X_{\max}\rangle$ values and their relation to all the evaluated extragalactic dipole positions.

For a more focused view, values of $\Delta\langle X_{\max}\rangle$ lesser than 1 g/cm^2 were excluded, resulting in the data shown in Figure 8.9a. Following this, Figure 8.9b specifically pinpoints the extragalactic dipole location associated with the highest $\Delta\langle X_{\max}\rangle$ value. Similarly Figure 8.9c displays $\Delta(\sigma X_{\max})$ values exceeding 1 g/cm^2 and Figure 8.9d identifies the extragalactic dipole location with the highest $\Delta(\sigma X_{\max})$ value.

These analyses collectively affirm that the position of an extragalactic dipole significantly influences both $\Delta\langle X_{\max}\rangle$ and $\Delta(\sigma X_{\max})$ values, thereby affecting the mass-dependent anisotropic behavior. This behaviour is a consequence of both the mass composition of cosmic rays and the position and amplitude of the extragalactic dipole. The strongest effect for both values has a single extragalactic dipole shown in Figure 8.9b and Figure 8.9d with its corresponding position on the sky map being $(l) >$ -135° and $(b) >$ 30°. The Figure 8.8 shows the complete list o 1005 tested dipoles.

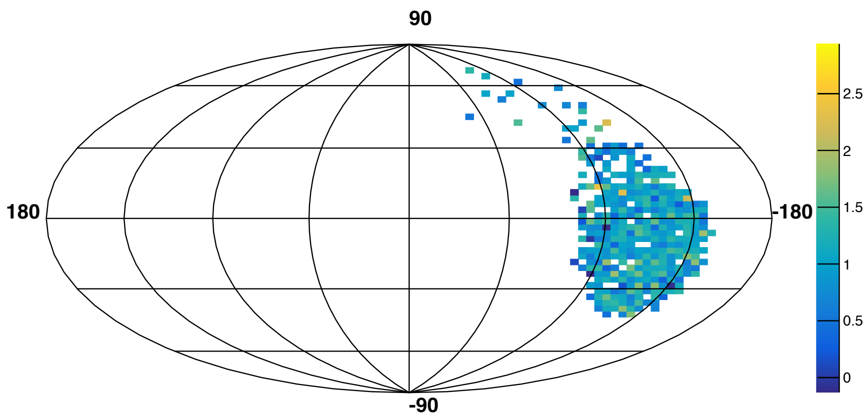

Figure 8.8: The directions of the 1005 possible extragalactic dipoles taken from [46], whose value is within 2σ of the observed Auger dipole in Galactic coordinates. Here the Z-axis results represent the on-off dipole $\Delta\langle X_{\max}\rangle$ values for each chosen dipoles position.

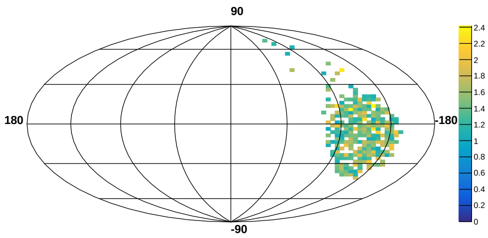

(a) Directions of the extragalactic dipole where $\Delta\langle X_{\mathrm{max}}\rangle > 1$ g/cm^2

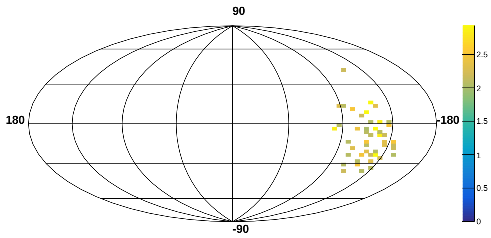

(b) Directions of the extragalactic dipole where $\Delta\langle X_{\mathrm{max}}\rangle > 2$ g/cm^2

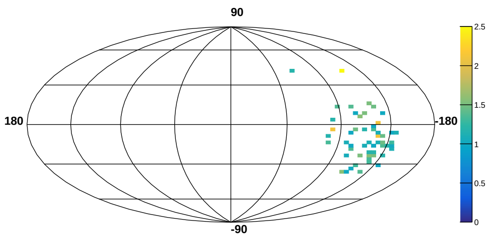

(c) Directions of the extragalactic dipole where $\Delta\sigma(X_{\mathrm{max}}) > 1$ g/cm^2

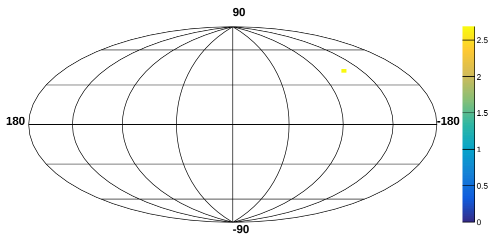

(d) Directions of the extragalactic dipole where $\Delta\sigma(X_{\mathrm{max}}) > 2$ g/cm^2

Figure 8.9: Directions of extragalactic dipoles for different thresholds of $\Delta\langle X_{\mathrm{max}}\rangle$ and $\Delta\sigma(X_{\mathrm{max}})$.

Conclusions

This diploma thesis was dedicated to reproduce the aspects of the mass-dependent anisotropy in arrival directions of cosmic rays with respect to the Galactic plane that was observed by the Piere Auger Observatory above energy of $10^{18.7}$ eV [8, 9]. Two following factors which can influence such observation were studied; mass composition of cosmic rays and the properties of the extragalactic dipole, assuming one particular model of the Galactic magnetic field (GMF). To closely analyze the above-mentioned effects, simulations using an open-source framework called CRPropa 3 in three-dimensional mode were used. For these simulations, the particles were back-tracked as antiparticles from Earth through the JF12 GMF (Section 2.2) to the edge of the Galaxy; in Chapter 5.1.

In the first analysis that was performed in Chapter 6, the methodology of on-off galactic-plane selection of simulated particles according to their arrival directions was applied as in [8, 9]. It resulted in non significant values of the change of average mass-dependent parameter $\Delta\langle X_{\mathrm{max}}\rangle < \pm\ 0.3$ g/cm^2 and its fluctuations $\Delta\sigma(X_{\mathrm{max}})$ = (0.2 ± 0.2) g/cm^2, for the most extreme case of the 50/50 mix of protons and iron nuclei, even for various ranges of energy. This is in contradiction with what was observed in [8, 9].

As the main result of the diploma thesis, a modified analysis was proposed and performed in Chapter 7. The methodology of on-off dipole selection was applied, based on the observation in [56]. The particles were divided according to their arrival directions with respect to excess and lack of the observed dipole in the right ascension. In such a particle division, values of $\Delta\langle X_{\mathrm{max}}\rangle = (2.7 \pm 0.3)$ g/cm^2 and $\Delta\sigma(X_{\mathrm{max}}) = (0.06 \pm 0.1)$ g/cm^2 were found for the most extreme case of the 50/50 mix of protons and iron nuclei. We did not obtain the magnitudes observed in [8, 9] even for such an event division; however, we showed that the mass-dependent anisotropy correlates with the size of the mixing of mass composition of cosmic rays when properties of one specific extragalactic dipole were assumed.

The final analysis done in Chapter 8 tests how much the mass-dependent anisotropy depends on the properties of an extragalactic dipole. The wide space of solutions for primary fractions and dipole properties obtained from the author of [46] was used for such a purpose, taking into account the effect of GMF using the JF12 model. The results using on-off dipole selection suggest that the properties of the extragalatic dipole affect both the values of $\Delta\langle X_{\mathrm{max}}\rangle$ and $\Delta(\sigma X_{\mathrm{max}})$ leading to the conclusion that the mass-dependent anisotropy of the arrival directions of particles is sensitive to the size of mixing of mass composition and also to the specific extragalatic dipole position, with the strongest effect for dipole directions of galactic (l) > -135° and (b) > 30°. Therefore, the maximal mass-dependent anisotropy signal can be obtained even for a not maximally mixed beam of primary particles for specific properties of the extragalactic dipole.

In light of recent advancements, I would like to mention the following study [57] which presents updated results relevant to the topics explored in this diploma thesis. These updated findings could potentially enhance the results, particularly in the context of the Galactic magnetic field and extragalactic dipole properties. While this study was published concurrently with the completion of this diploma thesis, its insights may offer additional perspectives or data that could enhance the conclusions drawn here, specifically regarding the mass composition of cosmic rays and the influence of the extragalactic dipole. Incorporating these recent findings in future iterations could lead to a more comprehensive conclusion.

Bibliography

[1] V. F. Hess, Über den ursprung der durchdringenden strahlung, Z. Phys. 14 (1913) 610.

[2] F. Fenu, The cosmic ray energy spectrum measured using the Pierre Auger Observatory, PoS ICRC2017 (2017) 486. doi:10.22323/1.301.0486.

[3] J. Linsley, Primary cosmic rays of energy 10^{17} to 10^{20} ev, the energy spectrum and arrival directions, in: International Cosmic Ray Conference, Vol. 4, 1963, p. 77.

[4] Pierre Auger Collaboration, Observation of a large-scale anisotropy in the arrival directions of cosmic rays above 8×10^{18} ev, Science 357 (6357) (2017) 1266–1270. doi:10.1126/science.aan4338.

[5] Pierre Auger Collaboration, Depth of maximum of air-shower profiles at the Pierre Auger Observatory: Measurements above $10^{17.2}$ eV and Composition Implications, PoS ICRC2017 (2017) 506. doi:10.22323/1.301.0506.

[6] N. Globus, et al., Propagation of high-energy cosmic rays in extragalactic turbulent magnetic fields: resulting energy spectrum and composition, Astronomy & Astrophysics 479 (1) (2008) 97–110. doi:https://doi.org/10.1051/0004-6361:20078653.

[7] R. A. Batista, et al., Crpropa 3—a public astrophysical simulation framework for propagating extraterrestrial ultra-high energy particles, Journal of Cosmology and Astroparticle Physics 2016 (05) (2016) 038–038. doi:10.1088/1475-7516/2016/05/038.

[8] E. Mayotte, et al., Indication of a mass-dependent anisotropy above $10^{18.7}$ ev in the hybrid data of the Pierre Auger Observatory (2022). doi:10.22323/1.395.0321.

[9] E. Mayotte, et al., Update on the indication of a mass-dependent anisotropy above $10^{18.7}$ ev in the hybrid data of the Pierre Auger Observatory, arXiv preprint arXiv:2303.16336 (2023).
URL https://arxiv.org/abs/2303.16336

[10] K.-H. Kampert, et al., Measurements of the cosmic ray composition with air shower experiments, Astroparticle Physics 35 (10) (2012) 660–678. doi:10.1016/j.astropartphys.2012.02.004.

[11] I. V. Dorman, Cosmic rays, Moscow Izdatel Nauka (Jan. 1981).

[12] A. Haungs, et al., Investigating the 2nd knee: The Kascade-Grande experiment, in: Journal of Physics: Conference Series, Vol. 47, IOP Publishing, 2006, p. 029. doi:10.1088/1742-6596/47/1/029.

[13] Pierre Auger Collaboration, Features of the energy spectrum of cosmic rays above 2.5×10^{18} ev using the Pierre Auger Observatory, Physical review letters 125 (12) (2020) 121106. doi:https://doi.org/10.1103/PhysRevLett.125.121106.

[14] P. Abreu, et al., The energy spectrum of cosmic rays beyond the turn-down around 10^{17} ev as measured with the surface detector of the Pierre Auger Observatory, The European Physical Journal C 81 (2021) 1–25. doi:https://doi.org/10.1140/epjc/s10052-021-09700-w.

[15] B. Peters, Primary cosmic radiation and extensive air showers, Il Nuovo Cimento (1955-1965) 22 (4) (1961) 800–819. doi:https://doi.org/10.1007/BF02783106.

[16] K. Greisen, End to the cosmic-ray spectrum?, Physical Review Letters 16 (17) (1966) 748. doi:https://doi.org/10.1103/PhysRevLett.16.748.

[17] G. T. Zatsepin, V. A. Kuz'min, Upper limit of the spectrum of cosmic rays, Soviet Journal of Experimental and Theoretical Physics Letters 4 (1966) 78. URL http://www.jetpletters.ru/ps/1624/article_24846.shtml

[18] I. Valino, The flux of ultra-high energy cosmic rays after ten years of operation of the Pierre Auger Observatory , PoS ICRC2015 (2016) 271. doi:10.22323/1.236.0271.

[19] C. Patrignani, K. Agashe, G. Aielli, C. Amsler, M. Antonelli, D. Asner, H. Baer, S. Banerjee, R. Barnett, T. Basaglia, et al., Review of particle physics (2016). doi:10.1088/1674-1137/40/10/100001.

[20] K. Greisen, Cosmic ray showers, Annual Review of Nuclear Science 10 (1) (1960) 63–108. doi:10.1146/annurev.ns.10.120160.000431.

[21] Pierre Auger Collaboration, Depth of maximum of air-shower profiles at the Pierre Auger Observatory. i. measurements at energies above $10^{17.8}$ eV, Phys. Rev. D 90 (2014) 122005. doi:10.1103/PhysRevD.90.122005.

[22] J. C. Mather, E. Cheng, et al., Measurement of the cosmic microwave background spectrum by the cobe firas instrument, The Astrophysical Journal 420 (1994) 439–444. doi:10.1086/173574.

[23] A. Bakalová, Connection between energy spectrum, mass composition and distribution of sources of extragalactic cosmic rays, Experimental Nuclear and Particle Physics, Master Thesis, ČVUT, fjfi. URL http://hdl.handle.net/10467/76304

[24] D. Kuempel, Extragalactic propagation of ultra-high energy cosmic rays (2014). arXiv:1409.3129.

[25] L. M. Widrow, Origin of galactic and extragalactic magnetic fields, Rev. Mod. Phys. 74 (2002) 775–823. doi:10.1103/RevModPhys.74.775.

[26] R. M. Crutcher, Magnetic fields in molecular clouds, Annual Review of Astronomy and Astrophysics 50 (2012) 29–63. doi:https://doi.org/10.1146/annurev-astro-081811-125514.

[27] M. S. Pshirkov, P. G. Tinyakov, et al., Deriving the global structure of the galactic magnetic field from faraday rotation measures of extragalactic sources, The Astrophysical Journal 738 (2) (2011) 192. doi:10.1088/0004-637x/738/2/192.

[28] E. Lopez-Rodriguez, Guerra, et al., The strength and structure of the magnetic field in the galactic outflow of Messier 82, The Astrophysical Journal 914 (1) (2021) 24. doi:10.3847/1538-4357/abf934.

[29] M. Ackermann, M. Ajello, et al., Detection of the characteristic pion-decay signature in supernova remnants, Science 339 (6121) (2013) 807–811. doi:10.1126/science.1231160.

[30] R. Jansson, G. R. Farrar, A new model of the galactic magnetic field, The Astrophysical Journal 757 (1) (2012) 14. doi:10.1088/0004-637x/757/1/14. URL http://dx.doi.org/10.1088/0004-637X/757/1/14

[31] J. Brown, et al., Rotation measures of extragalactic sources behind the southern galactic plane: New insights into the large-scale magnetic field of the inner Milky way, The Astrophysical Journal 663 (1) (2007) 258. doi:10.1086/518499.

[32] V. Heesen, R. Beck, M. Krause, R.-J. Dettmar, Cosmic rays and the magnetic field in the nearby starburst galaxy NGC 253-I. the distribution and transport of cosmic rays, Astronomy & Astrophysics 494 (2) (2009) 563–577. doi:https://doi.org/10.1051/0004-6361:200810543.

[33] K. Dolag, D. Grasso, V. Springel, I. Tkachev, Mapping deflections of extragalactic ultra high energy cosmic rays in magnetohydrodynamic simulations of the local universe, Nuclear Physics B-Proceedings Supplements 136 (2004) 234–243. doi:https://doi.org/10.1016/j.nuclphysbps.2004.10.030.

[34] K. Enqvist, Primordial magnetic fields, International Journal of Modern Physics D 7 (03) (1998) 331–349. doi:https://doi.org/10.1142/S0218271898000243.

[35] J. P. Conlon, F. V. Day, 3.55 keV photon lines from axion to photon conversion in the Milky Way and M31, Journal of Cosmology and Astroparticle Physics 2014 (11) (2014) 033. doi:10.1088/1475-7516/2014/11/033.

[36] Pierre Auger Collaboration, Nuclear Instruments and Methods in Physics Research Section A: Accelerators, Spectrometers, Detectors and Associated Equipment 798 (2015) 172–213. doi:https://doi.org/10.1016/j.nima.2015.06.058.

[37] Pierre Auger Collaboration, Timeline of the Pierre Auger Observatory, accessed: 2023-04-30 (2023).
URL https://www.auger.org/observatory/timeline-observatory

[38] J. Abraham, et al., The fluorescence detector of the Pierre Auger Observatory 620 (2-3) (2010) 227–251. doi:https://doi.org/10.1016/j.nima.2010.04.023.

[39] C. Bonifazi for the Pierre Auger Collaboration, The angular resolution of the Pierre Auger Observatory, Nuclear Physics B - Proceedings Supplements 190 (2009) 20–25, proceedings of the Cosmic Ray International Seminars. doi:https://doi.org/10.1016/j.nuclphysbps.2009.03.063.

[40] B. R. Dawson, H. Y. Dai, P. Sommers, S. Yoshida, Simulations of a giant hybrid air shower detector, Astroparticle Physics 5 (1996) 239–247. doi:10.1016/0927-6505(96)00024-2.

[41] Pierre Auger Collaboration, Evidence for a mixed mass composition at the 'ankle' in the cosmic-ray spectrum, Physics Letters B 762 (2016) 288–295. doi:https://doi.org/10.1016/j.physletb.2016.09.039.

[42] Pierre Auger Collaboration, Measurement of the cosmic-ray energy spectrum above 2.5×10^{18} ev using the pierre auger observatory, Physical Review D 102 (6) (2020) 062005. doi:https://doi.org/10.1103/PhysRevD.102.062005.

[43] R. A. Gideon, R. A. Hollister, A rank correlation coefficient resistant to outliers, Journal of the American Statistical Association 82 (398) (1987) 656–666. doi:10.1080/01621459.1987.10478480.

[44] T. W. Anderson, D. A. Darling, Asymptotic Theory of Certain "Goodness of Fit" Criteria Based on Stochastic Processes, The Annals of Mathematical Statistics 23 (2) (1952) 193 – 212. doi:10.1214/aoms/1177729437.

[45] D. Allard, J. Aublin, B. Baret, E. Parizot, What can be learnt from UHECR anisotropies observations, Astronomy & Astrophysics 664 (2022) A120. doi:10.1051/0004-6361/202142491.

[46] A. Bakalová, J. Vícha, P. Trávníček, Modification of the Dipole in Arrival Directions of Ultra-high-energy Cosmic Rays due to the Galactic Magnetic Field (3 2023). arXiv:2303.08766.

[47] Pierre Auger Collaboration, Realsimhybrid, https://www.auger.unam.mx/AugerWiki/RealSimHybrid, accessed: 2023-04-29 (2023).
URL https://www.auger.unam.mx/AugerWiki/RealSimHybrid

[48] S. Argiro, S. Barroso, J. Gonzalez, et al., The Offline software framework of the Pierre Auger Observatory, Nuclear Instruments and Methods in Physics Research Section A: Accelerators, Spectrometers, Detectors and Associated Equipment 580 (3) (2007) 1485–1496. doi:https://doi.org/10.1016/j.nima.2007.07.010.

[49] S. Ostapchenko, QGSJET-II: towards reliable description of very high energy hadronic interactions, Nuclear Physics B - Proceedings Supplements 151 (1) (2006) 143–146. doi:10.1016/j.nuclphysbps.2005.07.026.

[50] T. Pierog, I. Karpenko, J. M. Katzy, E. Yatsenko, K. Werner, EPOS LHC: Test of collective hadronization with data measured at the CERN large hadron collider, Physical Review C 92 (3) (sep 2015). doi:10.1103/physrevc.92.034906.

[51] F. Riehn, H. P. Dembinski, R. Engel, A. Fedynitch, T. K. Gaisser, T. Stanev, The hadronic interaction model sibyll 2.3c and feynman scaling (2017). arXiv:1709.07227.

[52] T. Pierog, M. Alekseeva, T. Bergmann, et al., First results of fast one-dimensional hybrid simulation of eas using Conex, Nuclear Physics B - Proceedings Supplements 151 (1) (2006) 159–162. doi:https://doi.org/10.1016/j.nuclphysbps.2005.07.029.

[53] T. R. Team, Root: A data analysis framework, accessed: 2023-04-29 (2023). URL https://root.cern.ch/

[54] K. Cooray, Generalized gumbel distribution, Journal of Applied Statistics 37 (1) (2010) 171–179. doi:10.1080/02664760802698995.

[55] M. De Domenico, M. Settimo, et al., Reinterpreting the development of extensive air showers initiated by nuclei and photons, Journal of Cosmology and Astroparticle Physics 2013 (7) (2013). arXiv:1305.2331, doi:10.1088/1475-7516/2013/07/050.

[56] Pierre Auger Collaboration, Large-scale cosmic-ray anisotropies above 4 EeV measured by the Pierre Auger Observatory, The Astrophysical Journal 868 (1) (2018) 4. doi:10.3847/1538-4357/aae689.

[57] A. Bakalová, J. Vícha, P. Trávníček, Modification of the dipole in arrival directions of ultra-high-energy cosmic rays due to the galactic magnetic field, Journal of Cosmology and Astroparticle Physics 2023 (12) (2023) 016. doi:10.1088/1475-7516/2023/12/016.

A CRPropa 3 python code

```
from crpropa import *

#Magnetic field
randomSeed = 42
B = JF12Field()
B.randomStriated(randomSeed)
B.randomTurbulent(randomSeed)

#primar
A =[1,2,7,26]
Z =[1,4,14,56]
name = ["p","He","N","Fe"]

#Loop for each primar
for i in range(len(A)):
    #Simulation Setup
    simulation = ModuleList()
    simulation.add(PropagationCK(B, 1e-5, 1 * pc, 1 * kpc))
    simulation.add(MaximumTrajectoryLength(1 * Mpc))

    #Create  module that sets the observer location
    observer = Observer()
    observer.add(ObserverLargeSphere(Vector3d(0), 20 * kpc))
    simulation.add(observer)

    #Generate particles from the source
    source = Source()
    source.add(SourcePosition(Vector3d(-8.5,0,0) * kpc))
    source.add(SourceIsotropicEmission() )

    #add partidle generator for source
    source.add(SourceParticleType(- nucleusId(Z[i], A[i])))
    source.add(SourcePowerLawSpectrum(3.16 * EeV,
                                      100 * EeV, -1))

    #Output and specific info to be writen to .txt
    output1 = TextOutput('JF12Backtracking_'+name[i],
                         +'_18.5-20.0.txt',
                         Output.Trajectory3D)

    output1.setLengthScale(kpc)
    output1.disableAll()
    output1.enable(Output.TrajectoryLengthColumn)
    output1.enable(Output.CurrentIdColumn)
    output1.enable(Output.CurrentEnergyColumn)
```

```
output1.enable(Output.CurrentPositionColumn)
output1.enable(Output.CurrentDirectionColumn)
output1.enable(Output.CreatedPositionColumn)
output1.enable(Output.CreatedDirectionColumn)
output1.enable(Output.SerialNumberColumn)

observer.onDetection(output1)

simulation.setShowProgress(True) #(tqdm)
simulation.run(source, 1000000) #n for gen.
```

B CRPropa 3 back-tracking simulation validation

As mentioned previously, the approach selected for CRPropa 3 in this study is the backtracking method. To verify the precision of the results produced, a comparison is conducted at an energy level of 8 EeV with the forward tracking method. The simulated particles used for this analysis are smaller in size consisting of 100,000 generated particles per element and are provided by [46].

Figure 10 and Figure 11 exhibit identical behaviour, confirming the consistency between the two propagation methods. In conclusion, the performance of CRPropa 3 is consistent between the backtracking and forward tracking methods. Allowing to use the backtracking method in the final product for this diploma thesis.

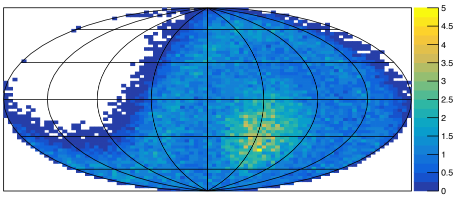

Figure 10: Forward tracking Mollweide projection of arrival directions in galactic coordinates, with Auger-Dipole. Z-axis represents the relative flux intensity. Energy cut 8 EeV up to 100 EeV.

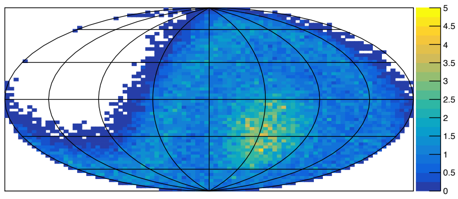

Figure 11: Back tracking Mollweide projection of arrival directions in galactic coordinates, with Auger-Dipole. Z-axis represents the relative flux intensity. Energy cut 8 EeV up to 100 EeV.

C Additional $\Delta\langle X_{\mathbf{max}}\rangle$ and $\sigma^2(\ln(\mathrm{A}))$ analysis

In this section, an additional analysis on the $\Delta\langle X_{\max}\rangle$ and $\sigma^2(\ln(\mathrm{A}))$ for 1005 extra-galatic dipole solutions used in Chapter 8 but instead uses the galactic on-off plane split, which results in no significant values.

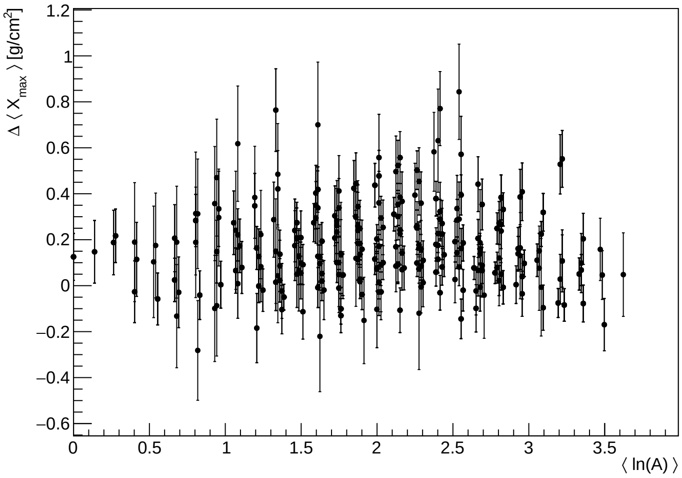

Figure 12: For energy above $10^{18.7}$ eV, all 267 possible mixed compositions of p, He, N and Fe with anisotropic distribution of arrival directions to the Galaxy are represented as a plot of $\Delta\langle X_{\max}\rangle$ versus $\langle\ln(\mathrm{A})\rangle$ using the on-off galactic plane split.

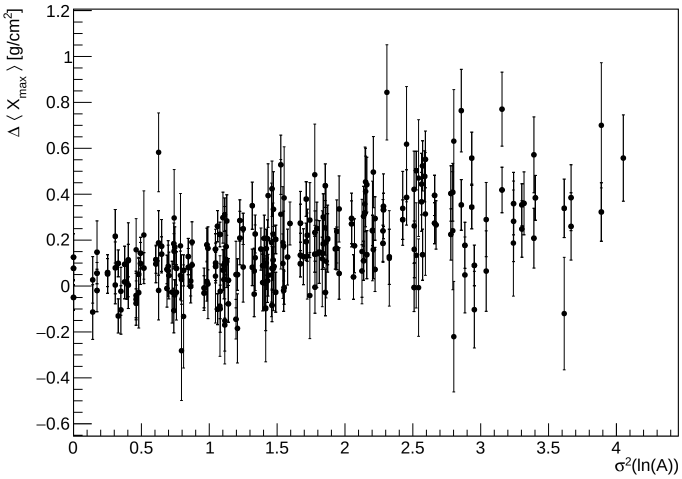

Figure 13: For energy above $10^{18.7}$ eV all 286 possible mixed compositions of p, He, N and Fe with anisotropic distribution of arrival directions to the Galaxy are represented as a plot of $\Delta\langle X_{\max}\rangle$ versus $\sigma^2(\ln(\mathrm{A}))$ using the on-off galactic plane split.